Dynamics of a single bubble in Newtonian and non-Newtonian fluids: Experimental and simulation approaches

International Journal of Multiphase Flow 174 (2024) 104789

Contents lists available at ScienceDirect

International Journal of Multiphase Flow

journal homepage: www.elsevier.com/locate/ijmulflow

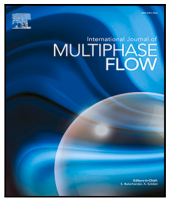

Dynamics of a single bubble in Newtonian and non-Newtonian fluids: Experimental and simulation approaches

Hauna Fathmadinda Hosen [a,*], Armin Shahmardi [b], Luca Brandt [b,c], Jannike Solsvik [a,*]

[a] Department of Chemical Engineering, NTNU – Norwegian University of Science and Technology, N-7491 Trondheim, Norway
[b] SeRC (Swedish e-Science Research Centre) and FLOW, Department of Engineering Mechanics, KTH Royal Institute of Technology, SE-100 44 Stockholm, Sweden
[c] Department of Energy and Process Engineering, NTNU – Norwegian University of Science and Technology, N-7491 Trondheim, Norway

ARTICLE INFO

Keywords:
Single bubble
Terminal velocity
Non-Newtonian
Shear-thinning
Fluid rheology
Bubble hydrodynamics

ABSTRACT

The intricate nature of non-Newtonian fluid rheology has raised notable attention, particularly in gas–liquid systems, where the dispersed bubbles may generate shear forces and change the shear-dependent viscosity of the surrounding liquid. While the effective shear rate, $\dot{\gamma}_{\text{eff}} = v_b/D_b$, is commonly used to approximate the shear-thinning viscosity around spherical bubbles, deviations may arise for deformed bubbles present in real systems. This work combines laboratory experiments and numerical simulations to investigate the evolution of a single rising bubble in three different systems: water, glycerol/water solutions characterizing viscous-Newtonian systems, and carboxymethyl cellulose (CMC) aqueous solutions exhibiting shear-thinning. The experiment was performed with bubble sizes of 1–9 mm using imaging techniques. The measured fluid rheology is modeled by the Carreau model, and used in 3D direct numerical simulations based on a diffuse interface approach. The shear-thinning behaviors are found to increase the bubble terminal velocity through two distinct mechanisms: reducing the apparent viscosity around the bubble and promoting the bubble deformation. The extent of the shear-thinning effect depends on the three dominating regimes under which different rheology parameters play a significant role. Finally, empirical models for bubble terminal velocity and drag coefficient are evaluated using two shear-thinning viscosity estimations, based on the effective shear rate and the average shear-thinning viscosity near the bubble interface. The good agreement between experimental and simulation results validates the proposed models.

1. Introduction

Gas bubbles dispersed in liquid media are found in various industries such as biorefinery and pharmaceutical production, where the fluid rheology is one of crucial parameters determining the performance of unit operations (Barba et al., 2022; Mastropietro et al., 2013). Unlike Newtonian liquids where the viscosity is shear-independent, systems with non-Newtonian liquids, which are commonly encountered in biochemical reactions, wastewater treatment, and biofuel processing (Chhabra, 2007; Rutz and Janssen, 2007; Doran, 2013), exhibit shear-dependent-viscosity, that may change the hydrodynamic properties of the bubbles, e.g., bubble size, deformation, instability, terminal velocity, drag, and eventually influence the effectiveness of the operation (Barnes et al., 1989; R. P. Chhabra, 2008). It is therefore important to investigate the evolution of a single rising bubble to understand better the effect of fluid rheology on the bubble hydrodynamics.

Semi-empirical relations have been proposed in the literature to reproduce the effect of the bubble size on its terminal velocity. One approach to estimate the terminal velocity is by a force balance for a single bubble that includes pressure gradient, added mass, drag, buoyancy and the Basset (history) forces (Darmana et al., 2009). This approach yields an implicit expression for the terminal velocity where the drag coefficient contained in the balance is a function of the bubble terminal velocity, which, therefore, requires an iterative computation. Another method results from the combination of the force balance and a wave analogy approaches (Fan and Tsuchiya, 1990), and distinguishes three regimes dominated by viscous, surface tension, and inertial forces. This method enables an explicit estimate of the terminal velocity as a function of bubble size and liquid properties. Liu et al. (2016) discussed that the three dominating regimes occur for small, intermediate, and large bubbles, respectively. Some remarkable improvements of the Fan and Tsuchiya (1990)'s expression were suggested by Maneri and Vassallo (2000) and Baz-Rodríguez et al. (2012), particularly in the viscous-dominated regime. Although some of the proposed expressions for the bubble terminal velocity were examined

* Corresponding authors.
E-mail addresses: hauna.f.hosen@ntnu.no (H.F. Hosen), jannike.solsvik@ntnu.no (J. Solsvik).

https://doi.org/10.1016/j.ijmultiphaseflow.2024.104789
Received 17 November 2023; Received in revised form 11 February 2024; Accepted 4 March 2024
Available online 7 March 2024

Nomenclature

Roman Letters

$\mathbf{n}$	Unit normal vector
$\mathbf{v}$	Velocity vector
$\mathbf{f_s}$	Surface tension forces
A	Projected area
c	Fan's model parameter determining the contribution between surface tension and inertia
C_D	Drag coefficient
D	Diameter
E	Aspect ratio
g	Gravitational acceleration
K	Maneri's model parameter
k	Flow consistency
K_b	Model parameter determining the contribution of viscosity
K_{b0}	Model constant determining K_b
n	Model parameter determining the contribution from viscosity, surface tension, and inertia
p	Power-law index
P	Pressure
R	Radius
S	Sphericity
t	Time
v	Velocity
y	Vertical position

Greek Letters

$\dot{\gamma}$	Shear rate
λ	Characteristic time constant
μ	Viscosity
ρ	Density
σ	Surface tension
ϕ	Indicator function distinguishing between gas and liquid phases
ϵ	Interface thickness
Γ	Velocity scale parameter
κ	Local curvature

Subscripts

$(1,2)$	1st and 2nd term of velocity
0	Property at low shear rate, or at initial state
b	Bubble property
cap	Capillary
dom	Property at specified domain
eff	Effective
e	Equivalent
exp	Experimental results
g	Gas phase property
l	Liquid phase property
lit	Results obtained from literature
max	Maximum value
min	Minimum value
mod	Results estimated by models
osc	Property at which oscillation occurs
sim	Simulation results
surf	Surface
t	Property at terminal state

Operators

Δ	Difference
∇	Vector differential operator

Dimensionless Numbers

Ca	Capillary number, $\frac{\mu v}{\sigma}$
Ar	Archimedes number, $\frac{gD^3\rho_l(\rho_l-\rho_g)}{\mu^2}$
Eo	Eötvös number, $\frac{\Delta\rho g D^2}{\sigma}$
Mo	Morton number, $\frac{\rho\mu_l^4\Delta\rho}{\rho_l^2\sigma^3}$
Re	Reynolds number, $\frac{\rho_l v D}{\mu_l}$
We	Weber number, $\frac{\rho_l v^2 D}{\sigma}$

Abbreviations

CMC	Carboxymetyl cellulose
CTAB	Cetrimonium bromide
HEC	Hydroxyl-ethyl cellulose
PAA	Polyacrylamide
VOF	Volume of fluid
XG	Xanthan gum

Statistical Terms

R^2	Coefficient of determination
SE	Standard error

by Celata et al. (2007), Liu et al. (2016), and Kure et al. (2021) to analyze their applicability, there seems to be no literature investigating the accuracy of the expressions by Maneri and Vassallo (2000).

The most common case of air bubbles in water was experimentally investigated by Tomiyama et al. (2002), Wu and Gharib (2002), Celata et al. (2007), and Liu et al. (2015, 2016) where a wide scattering of terminal velocity appears when the bubble size exceeds 1.37 mm. This condition seems to coincide with a transition from rectilinear to either helical or zigzag trajectory. Wu and Gharib (2002) revealed that such velocity scattering is caused by the different initial bubble deformation which depends on the ratio of the bubble size to the inner diameter of the needle tip. Their analysis about the dependency of terminal velocity on the initial bubble deformation is consistent with Liu et al. (2015) and Tomiyama et al. (2002). Liu et al. (2015) observed that the bubble rising speed increases with bubble deformation. This dependency was quantitatively examined by Tomiyama et al. (2002) who take into account the bubble aspect ratio in the expression for the terminal velocity to better fit the data in water from the experiments of Liu et al. (2016) and Celata et al. (2007). In systems with viscous-Newtonian fluids, Liu et al. (2015, 2016) analyzed the effect of fluid viscosity on strengthening the bubble's resistance to deform, resulting in higher bubble aspect ratio compared to the water. They found that the terminal velocity models of Tomiyama et al. (2002) and Ishii and Chawla (1979) give the best prediction to their water and glycerol systems, respectively.

Experiments in non-Newtonian fluids were performed by Chehata (2004) and Soto (2008) to study the effect of shear-thinning inelastic and viscoelastic properties on the bubble shape. Soto (2008) observed the bubble shape in shear-thinning inelastic fluids to resemble the one obtained in viscous-Newtonian fluids. While most literature defines the bubble shape from its oblateness, i.e., aspect ratio, Zhang et al.

(2022) introduced an additional parameter, i.e., bubble sphericity. Another concern is related to the bubble trajectory. Hassan et al. (2008) demonstrate a two-fold effect of shear-thinning liquid on the bubble trajectory. Small bubbles tend to lower horizontal motions whereas the opposite is true for large bubbles whose spiralling motion increases with the liquid shear thinning. The effect of shear-thinning behavior on the bubble terminal velocity was qualitatively studied by Amirnia et al. (2013), Li et al. (2018), and Xu et al. (2019) by means of experiments with different non-Newtonian solutions. Nonetheless, further analyzes on empirical expressions are required to quantify the shear-thinning effect on the bubble dynamics. Table 1 summarizes existing literature of single bubbles rising in stagnant Newtonian or non-Newtonian fluids. In most literature with non-Newtonian cases, the rheology was assumed to follow a power-law model, i.e., inelastic non-Newtonian fluids. Furthermore, the estimation of the shear rate, $\dot{\gamma}$, at low Reynolds number was mostly expressed as the ratio of a characteristic velocity to a bubble length scales, which were taken from the bubble rising speed and the bubble size, giving $\dot{\gamma} = v_b/D_b$. However, this model assumes a spherical shape, and deviations may occur for deformed bubbles which are normally present in any real systems.

In this work, the effect of the liquid shear-thinning on the bubble terminal velocity is examined for different bubble sizes with particular focus on:

- examining the conditions where the effective shear rate, $\dot{\gamma} = v_b/D_b$, is applicable,
- estimating the shear-thinning viscosity near the bubble interface whose the applicability is compared to the effective viscosity,
- analyzing the effect of rheology parameters on the bubble terminal velocity within the viscous, surface tension, and inertial dominated regimes,
- evaluating the pre-existing expressions of terminal velocity to suggest a model that fits the experimental results for Newtonian and non-Newtonian cases.

Experimental investigations and 3D direct numerical simulations (DNS) are integrated to assess two shear-thinning viscosity estimations, based on (i) the effective shear-rate and (ii) the average shear-thinning viscosity near the bubble interface. The experimental setup and simulation method are explained in Section 2. The results are discussed in Section 3, encompassing experimental observations, simulation results, and drag analyses in Sections 3.1, 3.2, and 3.3, respectively. Finally, the main conclusions are summarized in Section 4.

2. Experimental setup and simulation method

2.1. Column design and bubble generation

Fig. 1 illustrates the experimental configuration where a single air bubble is injected by a syringe pump and released from a needle located at the bottom of a plexiglass column. The syringe pump is operated with injection rates of 0.5–10 μL/h to generate one single bubble for each run. The needle is made from glass or metal with various inner diameters to cover bubble sizes of 1–9 mm, in which the rectilinear, helical, and zigzag trajectories are expected to appear. The rising bubble is imaged by a static high-speed camera after reaching 34.5 cm from the bottom of the column for around 0.3–1.5 s. A light source is provided from the back side of the column where a diffuser paper is attached to distribute the light more homogeneously and reduce any possible reflections caused by the column wall or the bubble surface. The column is designed with a cross-sectional area of 12 × 12 cm^2, i.e., > 10 times larger than the bubble sizes, to eliminate the wall effects. All experiments were performed with a liquid height of 80 cm at room temperature of 22° C. More details on the experimental configuration are specified in Table 2.

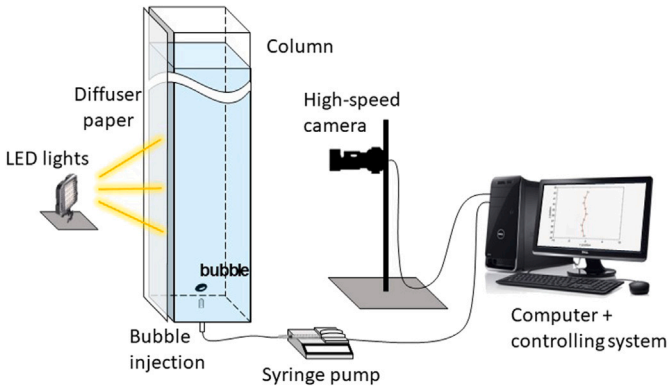

Fig. 1. Experimental Setup.

2.2. Liquid preparation and rheology measurement

The dynamics of single air bubbles are investigated for deionized water, glycerol/water solutions, and carboxymethyl cellulose (CMC) aqueous solutions to exhibit low- and high-viscous Newtonian, and non-Newtonian (shear-thinning) behavior. The preparation of the glycerol/water solution required two-hour mixing of glycerol 99.7% (with a density of 1220 kg/m^3, supplied by VWR-Avantor) and deionized water, followed by an overnight resting time to remove small bubbles generated during mixing. The CMC aqueous solution was prepared by dissolving ultra-highly-viscous CMC (highly purified CMC with viscosities of 1.5–4.5 Pa s, supplied by Sigma-Aldrich, Norway) in deionized water at around 55°C for overnight. The viscosities of all fluids were measured using a cylindrical rheometer (Physcia MCR 301, Anton Paar GmbH, Austria) with shear rates ranging from 0.01–1000 1/s. Each measurement with the rheometer started after a resting time of 10 min for the sample to reach thermal equilibrium at 22°C. Fig. 2 presents the measured viscosities, μ, against the shear rates, $\dot{\gamma}$, which are fitted to the Carreau model:

$$\mu_l = \mu_0 \left[1 + (\lambda\dot{\gamma})^2\right]^{\frac{p-1}{2}} \quad (1)$$

where μ_0, λ, and p denote the zero-shear viscosity, characteristic time constant, and power-law index, respectively. The fitted values are listed in Table 3. The density, ρ, and the surface tension, σ, were measured using a density meter (Anton Paar DMA 5000) and a ring tensiometer (Sigma Attension 701). The physical properties of the 3 working fluids are also presented in Table 3.

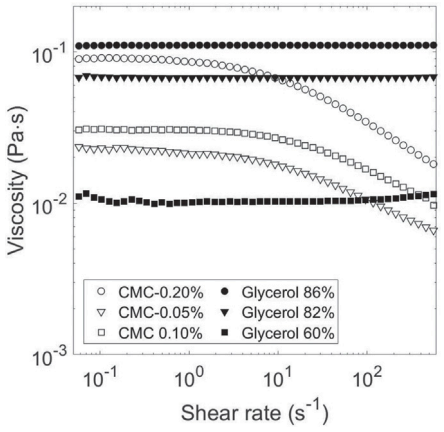

Fig. 2. Viscosity as a function of shear rate for different fluids.

Table 1
Literature overview of experimental and analytical investigation on single rising bubbles for Newtonian and non-Newtonian cases.

Reference	Fluid	Bubble size (mm)	Rheology model	Study method	Remarks
Haberman and Morton (1953)	water varsol turpentine glycerol corn syrup mineral oil	0.3–63.0 0.2–16.0 0.3–6.0 1.0–14.0 0.4–26.0 3.5–14.0	– – – – – –	experiment in 3 columns: $91 \times 91 \times 91$ cm^3 $30 \times 30 \times 107$ cm^3 $2.5 \times 2.5 \times 61$ cm^3	$v_t = \frac{1}{18}\frac{\Delta\rho g D_e^2}{\mu_l}\left[\frac{3\mu_l+3\mu_g}{2\mu_l+3\mu_g}\right]$ applicable for small bubbles
Fan and Tsuchiya (1990)[a]	water varsol turpentine glycerol corn syrup mineral oil	0.2–63	–	semi-empirical model development	$v_t = \left[\frac{1}{v_{b1}{}^n} + \frac{1}{v_{b2}{}^n}\right]^{-1/n}$ $v_{b1} = \frac{\rho_l g D_e^2}{K_b \mu_l}$; $v_{b2} = \sqrt{\frac{2c\sigma}{\rho_l D_e} + \frac{gD_e}{2}}$ $K_b = max(12, K_{b0} Mo^{-0.038})$ $K_{b0} = 14.7$ (aqueous solutions) $K_{b0} = 10.2$ (organic solutions) $c = 1.2$ (mono-component liquids) $c = 1.4$ (multi-component liquids) $n = 1.6$ (clean system) $n = 0.8$ (contaminated system)
Maneri and Vassallo (2000)	Newtonian	0.2–20	–	semi-empirical model development	v_t by Fan and Tsuchiya (1990) $K_b = K\left(1.0 - e^{-5.31\times10^{10}Mo}\right)\left(\frac{D_e}{D_o}\right)^a$ $D_o = 2.0\left[\frac{\sigma}{\Delta\rho g}\right]^{1/2}$; $K = 148$ or 60 $a = 0.425$; $n = 8.0$; $c = 1.0$ or 1.4
Raymond and Rosant (2000)	glycerol	1.5–13	–	experiment in $30 \times 20 \times 50$ cm^3	
Rodrigue (2001)	Newtonian	–	–	semi-empirical model development	$v_t = \left[\frac{D_e^2\rho^2}{\sigma\mu}\right]^{-1/3}\frac{aF^b}{[1+cF]^d}$ $F = g\left(\frac{D_e^8\rho^5}{\sigma\mu^4}\right)^{1/3}$ $a = 1/2$; $b = 1$; $c = 0.0185$; $d = 3/4$
Rodrigue (2002)	shear-thinning	0.3–27.0	Power law	semi-empirical model development	$v_t = D_e^{\frac{p+1}{p}}\left[\frac{k_r k}{\rho g}\right]^{-1/p}$; $k_r = 39.9$ $0.013 \le k \le 6.25$ $[Pa \cdot s^p]$ $0.448 \le p \le 1.0$
Tomiyama et al. (2002)	water	0.6–11	–	experiment in $10 \times 10 \times 20$ cm^3	$v_t = \frac{sin^{-1}\sqrt{1-E^2}-E\sqrt{1-E^2}}{1-E^2}\sqrt{\frac{8\sigma E^{4/3}}{\rho D_e} + \frac{\Delta\rho g D_e}{2\rho}\frac{E^{2/3}}{1-E^2}}$
Wu and Gharib (2002)	water	1.0–2.1	–	experiment in $15 \times 15 \times 61$ cm^3	
Zhang et al. (2008b)	glycerol sucrose	2.7–5.2 2.5	– –	experiment in $21 \times 21 \times 60$ cm^3	
Wenyuan et al. (2010)	PAA CMC	5.2–6.9 6.1–7.5	Power law Power law	experiment in $15 \times 15 \times 50$ cm^3	simplified shear rate, $\dot{\gamma} = \frac{v_t}{D_e E}$
Zhang et al. (2010)	CMC XG HEC	4.0–4.2 2.3 2.8–3.1	Carreau Carreau Carreau	experiment in $21 \times 21 \times 60$ cm^3 & VOF simulation	simplified shear rate, $\dot{\gamma} = \frac{2v_t}{D_e E}$
Amirnia et al. (2013)	XG CMC	0.1–1.8 0.2–2.1	Carreau & Power law	experiment in $27 \times 30 \times 240$ cm^3	simplified shear rate, $\dot{\gamma} = \frac{v_t}{D_e}$
Liu et al. (2015, 2016)	water glycerol	0.5–11.0 0.5–24.0	– –	experiment in $15 \times 15 \times 50$ cm^3	
Aoyama et al. (2016)	glycerol	0.7–6.0	–	experiment in $20 \times 20 \times 60$ cm^3	
Baz-Rodríguez et al. (2012)	pure liquids	0.3–60	–	semi-empirical model development	$v_t = \left[\frac{1}{v_{T1}{}^2} + \frac{1}{v_{T2}{}^2}\right]^{-1/2}$ $v_{T1} = v_{T,pot}\sqrt{1 + 0.73667\frac{\sqrt{gD_e}}{v_{T,pot}}}$; $v_{T2} = \sqrt{\frac{3\sigma}{\rho_l D_e} + \frac{gD_e\Delta\rho}{2\rho_l}}$ $v_{T,pot} = v_{b1}$ (Fan and Tsuchiya, 1990) with $K_b = 36$ (Levich, 1962)
Oshaghi et al. (2019)	glycerol CMC	2.2–9.5 2.2–9.5	– Power law	experiment in $12 \times 12 \times 50$ cm^3	bubble detachment velocity as the main focus
Xu et al. (2019)	PAA XG	0.7–6.0 1.5–7.0	Carreau Carreau	experiment in $10 \times 10 \times 30$ cm^3	simplified shear rate, $\dot{\gamma} = \frac{v_t}{D_e}$

(*continued on next page*)

Table 1 (*continued*).

Reference	Fluid	Bubble size (mm)	Rheology model	Study method	Remarks
Mahmoudi et al. (2019)	water kerosene	1.0–15.0 1.0–15.0	– –	experiment in $15 \times 15 \times 150$ cm^3	$v_t = a_1 \left[\frac{1}{v_{T1}{}^2} + \frac{1}{v_{T2}{}^2}\right]^{-a_2}$ $a_1 = 1.1089; a_2 = 0.5653$(water) $a_1 = 1.0611; a_2 = 0.5247$(kerosene) v_{T1} & v_{T2} follow Baz-Rodríguez et al. (2012)
Islam et al. (2020)	sucrose XG	2.5–17.0 2.5–17.0	– Power law	VOF simulation	
Battistella et al. (2020)	shear-thinning	0.5–4.0	Power law	VOF simulation	
Li et al. (2022)	PAA glycerol	1.2–9.7 1.2–9.7	Power law –	experiment in $8 \times 8 \times 100$ cm^3	simplified shear rate, $\dot{\gamma} = \frac{v_t}{D_e}$
Ravisankar et al. (2022)	PAA glycerol	2.7–8.3 2.7–8.3	Power law –	experiment in $5 \times 5 \times 40$ cm^3	simplified shear rate, $\dot{\gamma} = \frac{v_t}{D_e/2}$
Mahmoudi et al. (2022)	Newtonian, shear-thinning & shear-thickening	2.0–6.0	Power law	VOF simulation	simplified shear rate, $\dot{\gamma} = \frac{v_t}{D_e}$ $Mo_{\text{non-Newtonian}} = \frac{g^{3n-2}k^4}{\rho_l^{2-n}\sigma^{n+2}}$

CMC: carboxymethyl cellulose, XG: xanthan gum, PAA: polyacrylamide, HEC: hydroxyl-ethyl cellulose, VOF: volume of fluid, Mo: Morton number.
[a] v_{b1}: the dominance of viscosity & buoyancy over small-spherical bubble motion, analytically investigated by Haberman and Morton (1953)- and Rybczynski (1911), Stokes et al. (1851), and Levich (1962) with K_b = 12, 18, and 36, respectively.
v_{b2}: the dominance of surface tension (1st term) & buoyancy (2nd term) over intermediate-to-large bubble motion, analytically investigated by Mendelson (1967) with $c = 1$.

Table 2
Experimental configuration.

Aspect	Parameter	Specification
Column design	Column dimension	$12 \times 12 \times 100$ cm^3
	Liquid height	80 cm
Bubble generation	Syringe pump type	KdScientific Legato200
	Syringe volume	1 mL, 5 mL, 10 mL
	Injection rate	0.5–10 μL/hr
	Desirable bubble sizes, D_e	1–9 mm
	Inner diameter of the capillary tip, D_{cap}	20 μm–8 mm
	Needle material	glass for D_{cap} = 20 μm–4 mm metal for D_{cap} = 700 μm–8 mm
Image acquisition	Camera	Photron FASTCAM MINI AX100
	Frame size	8×8 cm^2
	Frame rate	500–1000 fps
	Shutter speed	1/12000–1/18000 s
	Resolution	1024×1024 px^2
	Observation time	300–1500 ms
	Controlling software	National Instruments LabVIEW 2021 SP1

Table 3
Physical and rheological properties.

Fluid	Carreau parameters			ρ(kg/m^3)	σ(mN/m)
	p	λ(s)	μ_0(Pa s)		
CMC 0.05 wt% in water	0.7142	0.12	0.022	998.00	71.10
CMC 0.10 wt% in water	0.7057	0.11	0.030	998.23	71.38
CMC 0.20 wt% in water	0.6845	0.24	0.090	998.66	71.62
Glycerol 60 wt% in water	1	0	0.011	1153.71	56.06
Glycerol 82 wt% in water	1	0	0.068	1213.00	59.88
Glycerol 86 wt% in water	1	0	0.110	1223.27	60.01

2.3. Analysis of bubble properties

All images obtained from the experiment were treated using an image processing algorithm in MATLAB (2021a) to determine the bubble properties as follows:

1. Contrast enhancement: subtracting images by the background using 'imcomplement',
2. Bubble edge detection: estimating the bubble edge by finding the local threshold using 'graythresh',
3. Binarization: converting images from RBG to binary format using 'imbinarize',
4. Filling: filling the white area inside bubble, that appears due to light reflection, using 'bwareaopen',
5. Imcomplement: switching the black and white areas in the binary image using 'imcomplement',
6. Small dots removal: removing white small areas appearing in the image with the same principle as filling by using 'bwareaopen',
7. Data extraction: extracting the data of bubble properties using 'regionprops'.

The bubble size is determined by estimating the volume equivalent diameter, D_e, given as

$$D_e = \sqrt[3]{D_{max}^2 \times D_{min}} \tag{2}$$

where D_{max} and D_{min} denote the major and minor axes lengths, respectively. These parameters are taken from the longest and shortest lengths of the projected area of the bubble, as illustrated in Fig. 3.

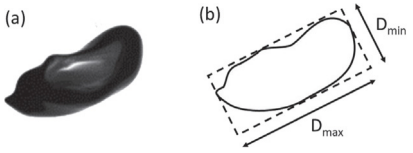

Fig. 3. (a) Bubble captured by the camera, (b) projected area of the bubble.

The bubble shape is defined in terms of the aspect ratio, E, and the sphericity, S, expressed as

$$E = \frac{D_{min}}{D_{max}}; \quad S = \sqrt{\frac{4\pi A}{\text{perimeter}^2}} \tag{3}$$

Since the bubble area, A, is quantified by the number of pixels, the bubble perimeter is computed as the averaged number of pixels between the inner perimeter and the outer perimeter of the bubble edge.

The bubble terminal velocity, v_t, is considered to be the same as the vertical velocity component (Liu et al., 2015, 2016; Kure et al., 2021) which is estimated as

$$v_{t,i} = \frac{y_{i+1} - y_i}{\Delta t} \tag{4}$$

where i denotes the ith time step, y is the vertical position of the bubble, and Δt is the time difference between the two consecutive vertical positions. The conversion of the unit length from pixel to millimeter was obtained from a calibration using a sphere with known diameter. For this purpose, spheres made of metal with diameters of either 3 mm, 4 mm, and 10 mm were used in the calibration, resulting in approximately the same value of 0.0791 mm/pixel.

2.4. Simulation method

For the simulations presented here, the interface between the two immiscible phases is captured by means of the Accurate Conservative Diffuse Interface (ACDI) method introduced by Jain (2022) where an indicator function, ϕ, is employed to distinguish between the two phases. The value of the indicator function varies from zero in the liquid phase to unity in the gas phase, smoothly but abruptly within a finite interface thickness, ϵ. The level-set of $\phi = 0.5$ is considered as the sharp interface limit between the phases. The evolution of the order parameter, thus the motion of the interface is captured by solving the following advection–diffusion equation:

$$\frac{\partial \phi}{\partial t} + \nabla \cdot (\mathbf{v}\phi) = \nabla \cdot \left[\Gamma \left(\epsilon \nabla \phi - \phi(1-\phi) \frac{\nabla \phi}{|\nabla \phi|} \right) \right], \tag{5}$$

where Γ is a velocity scale parameter, and $\mathbf{v}$ is the fluid flow velocity field.

The fluid flow is the solution of the incompressible Navier–Stokes equation:

$$\frac{\partial (\rho \mathbf{v})}{\partial t} + \nabla \cdot (\rho \mathbf{v}\mathbf{v}) = -\nabla P + \nabla \cdot \left[\mu (\nabla \mathbf{v} + \nabla \mathbf{v}^T) \right] + \rho \mathbf{g} + \mathbf{f}_s, \tag{6}$$

where P is the pressure, $\mathbf{g}$ is the gravitational acceleration, and $\mathbf{f}_s$ represents the surface tension forces at the interface of the two phases. In this work, the Continuous Surface Force (CSF) formulation is used to compute the interfacial forces as $\mathbf{f}_s = \sigma \kappa \nabla \phi$ based on a surface tension coefficient, σ, normal vector, $\mathbf{n} = \nabla\phi/|\nabla\phi|$, and local curvature, $\kappa = -\nabla \cdot \mathbf{n}$ (Brackbill et al., 1992).

In Eq. (6), ρ and μ are density and dynamic viscosity field varying from ρ_l and μ_l in the liquid phase to ρ_g and μ_g in the gas phase. The local values are obtained using a linear interpolation between the corresponding values in the two phases:

$$\rho = \phi\rho_g + (1-\phi)\rho_l, \quad \mu = \phi\mu_g + (1-\phi)\mu_l. \tag{7}$$

The shear-thinning effects are included by following the Carreau model introduced in Eq. (1) to compute the dynamic viscosity of the liquid phase, μ_l, which therefore changes with the local shear rate.

2.5. Simulation setup and numerical treatment

Fig. 4 illustrates a schematic of the simulation setup. A three-dimensional spherical bubble with radius R_0 is initially placed at the center of the bottom plane of the simulation box of size $[0, 18R_0] \times [0, 18R_0] \times [0, 142.8R_0]$. All the equations are discretized on a uniform Cartesian mesh consisting of 512 × 512 × 4096 grid points. A second order finite difference central scheme is employed for the spatial discretization whereas the Adams–Bashforth scheme is used for the temporal integration. The incompressibility constraint is imposed by employing the fractional-step method for two-fluid systems as introduced by Dodd and Ferrante (2014). The largest Courant number, i.e., CFL number, used in this simulation is 7.1×10^{-3}, which is smaller than the critical CFL ≤ 0.05 suggested by Cifani (2019) for fast computations, i.e., small enough to ensure the stability in the numerical simulations. Finally, for all the variables, periodic boundary condition is considered in all the three directions. The baseline code has been extensively validated in previous works and is available as a public repository (Crialesi-Esposito et al., 2023; Scapin et al., 2022; Bazesefidpar et al., 2022). The grid convergence was also verified at double resolution, which gives identical results to the ones presented in this study.

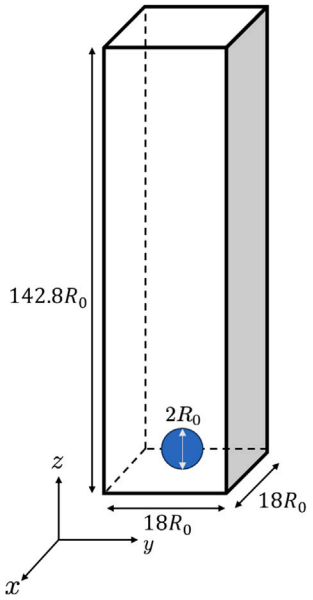

Fig. 4. Schematic of the simulation setup.

3. Results and discussion

In this work, the dynamics of single air bubbles in stagnant liquid are investigated through experiments and simulations. The experimental results are discussed in Section 3.1 where these are compared to existing results in the literature. These data are evaluated to obtain

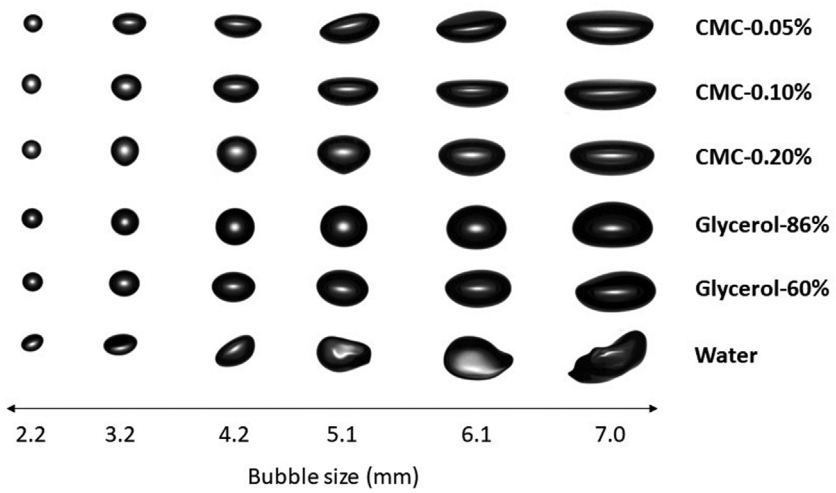

Fig. 5. Visualization of bubble shape for various sizes in different liquids.

empirical expressions of terminal velocity for Newtonian and non-Newtonian cases. The effect of shear-thinning is analyzed further by examining some representative cases through 3D direct numerical simulations, whose results are discussed in Section 3.2. Finally, a group of dimensionless numbers representing the bubble terminal velocity, bubble deformation, and fluid properties are analyzed in Section 3.3 where an estimate of the drag is suggested.

The experimental observations comprising bubble shape, trajectory, and terminal velocity are analyzed for water, glycerol–water solutions, and aqueous solutions of CMC within bubble equivalent diameters of $D_e \approx 1-9$ mm. The visual comparison of the bubble shape in Newtonian and non-Newtonian systems is presented in Section 3.1.1, highlighting the variations in bubble deformation and the relevant bubble shape parameters to be considered in terminal velocity expressions. The bubble trajectory for CMC cases is characterized by the time evolution of the bubble motion, terminal velocity, equivalent diameter, and aspect ratio as explained in Section 3.1.2. In Section 3.1.3, three regimes corresponding to three different dominating forces, i.e., viscous-, surface tension-, and inertial forces, are discussed in relation with the bubble deformation, trajectory, and terminal velocity. Before analyzing the effect of shear-thinning on each dominating force, the expressions for the terminal velocity in the literature are initially examined for Newtonian systems in Section 3.1.3.1. Furthermore, a comparative analysis between the current work and existing literature data is discussed in this section to reveal how the terminal velocity may vary based on different experimental setups. The most predictive model is then evaluated for non-Newtonian fluids and discussed in Section 3.1.3.2. This evaluation includes an extension of the literature expressions for the terminal velocity to incorporate the shear-thinning rheology, considering two different estimation approaches for the shear-thinning viscosity effect.

3.1. Experimental investigation

3.1.1. Bubble shape

The bubble shape can be categorized into different types: spherical, ellipsoidal, spherical-cap, oblate, prolate, and teardrop (Zenit and Feng, 2018; Xu et al., 2019). As visualized in Fig. 5, the bubble with $D_e \approx 2$ mm remains spherical in all systems except for the case of water where it starts to resemble an ellipsoidal shape. Among the Newtonian fluids, the bubble deforms more as its size increases. This can be explained by the Capillary number, $Ca = \frac{\mu v_t}{\sigma}$, that represents the relative importance of viscous forces to surface tension forces. The reference velocity is often taken to be the shear rate times the bubble size, $v_t \approx \dot{\gamma} D_e$. When Ca increases, e.g., due to an increase in D_e or viscosity as seen in Fig. 6 (a), the effect of the surface tension force is less significant than the viscous force, resulting in the bubble to lose its capability to stay spherical. As indicated in Fig. 6 (b), the aspect ratio E is found to decrease with Ca. Here, $E = 1$ represents a spherical shape and $E < 1$ indicates a deformed shape. The decrease in E with Ca occurs consistently for all Newtonian cases with different decrease rates, i.e., steeper curves are obtained for lower glycerol concentrations.

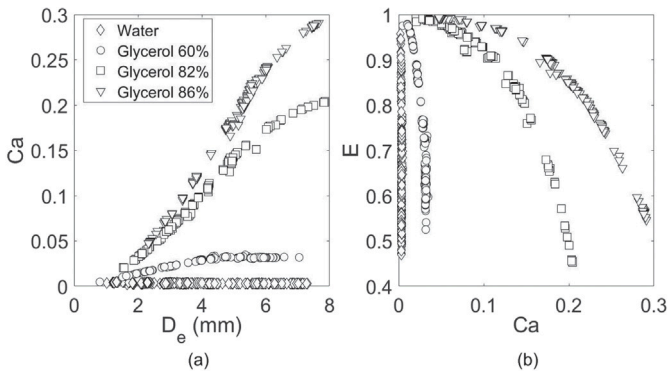

Fig. 6. (a) Capillary numbers as a function of D_e, and (b) E as a function of Capillary numbers for different Newtonian fluids.

Compared to the Newtonian fluids where larger bubbles exhibit spherical-cap or irregular-oblate (referred to as 'wobbly') shapes, as shown in Fig. 5 for 7 mm bubble in Glycerol 86% and water, the bubble rising in CMC solutions seems to deform differently, with a pointed tip appearing at the bottom of the bubble, known as the cusp. Zenit and Feng (2018) explains the reason behind the cusp formation as a result of the negative wake flowing downward under the bubble. This cusp is visible in CMC 0.2% for initial bubble size between $D_e \approx 3.2$ mm and $D_e \approx 5.1$ mm. As the CMC concentration decreases, the cusp becomes less observable which may indicate that the negative wake is weaker and tends to disappear.

The values of E are known to decrease with D_e for Newtonian systems (Raymond and Rosant, 2000; Wu and Gharib, 2002; Tomiyama et al., 2002; Liu et al., 2016; Aoyama et al., 2016; Kure et al., 2021). This pattern is similarly found for non-Newtonian systems, which are presented in Fig. 7 (a)–(c). For small bubbles, $D_e \leq 2$ mm, all CMC solutions result in $E \approx 1$, i.e., almost perfectly spherical shape. As the bubble size increases, E decreases, implying that the bubble deforms to a greater extent. Note however that for CMC 0.2%, there is a

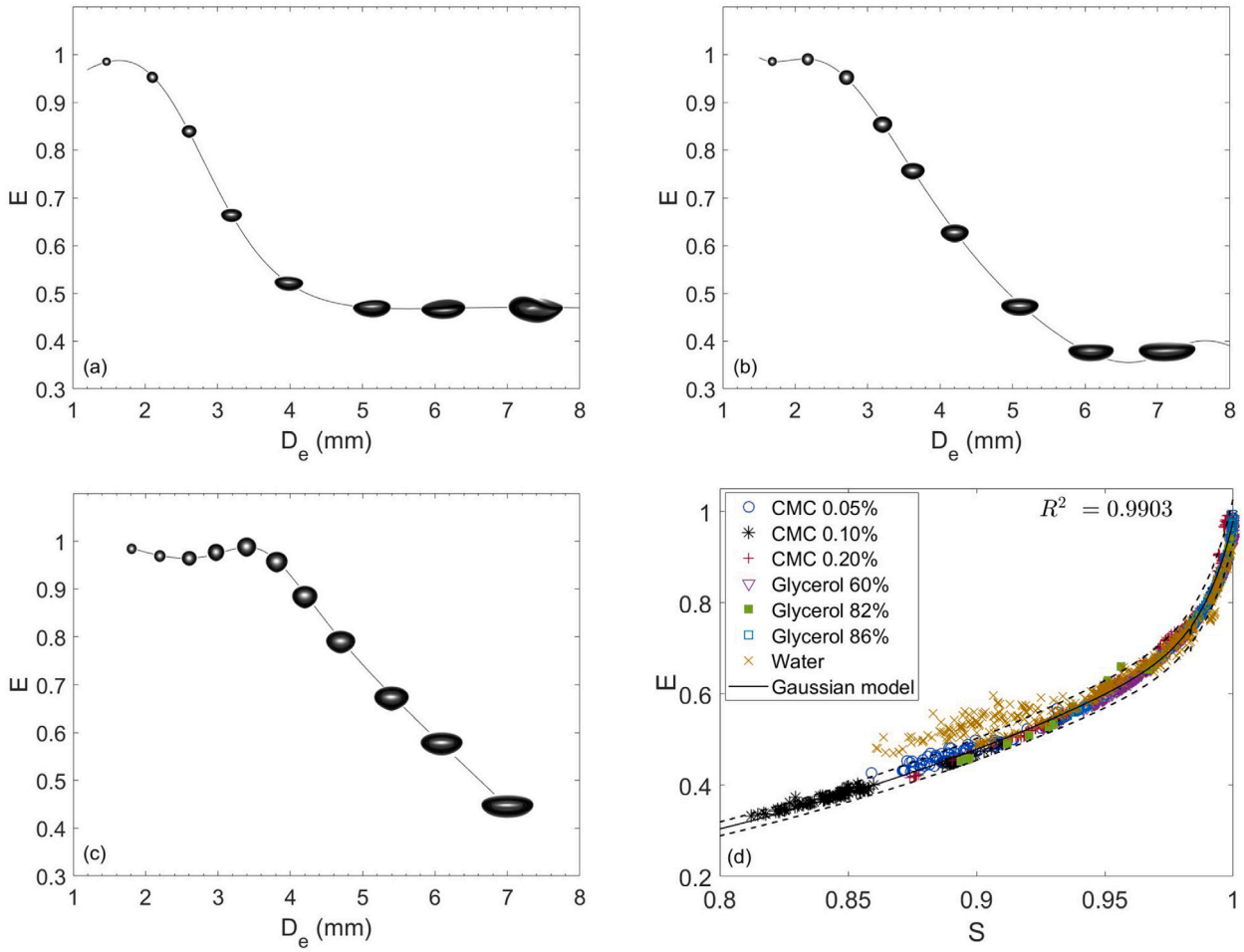

Fig. 7. Visualization of bubble shape and the corresponding aspect ratio as a function of bubble equivalent diameter for (a) CMC 0.05%, (b) CMC 0.10%, (c) CMC 0.20%, and (d) bubble aspect ratio as a function of bubble sphericity. The dashed-lines in (d) represent ±5% of the Gaussian model in Eq. (8) and R^2 is the coefficient of determination which represents the goodness of fit of Eq. (8).

slight increase of E for $D_e \approx 2.6$–3.5 mm at which a cusp emerges. The decreasing trend of E begins at a smaller D_e for lower CMC concentration, with $D_e \approx 1.8$, 2.2, and 3.5 mm for CMC 0.05%, 0.1%, and 0.2%, respectively. This indicates that higher CMC concentrations increase the tendency of the bubble interface to remain spherical. The E values keep decreasing until they reach a constant value of $E \approx 0.48$ and $E \approx 0.40$ for the two lowest CMC concentrations. These values are obtained when $D_e \geq 5$ mm and $D_e \geq 6$ mm, respectively. Conversely, E values for CMC 0.2% keep decreasing even after $D_e \geq 6$ mm. This may indicate that the more prominent shear-thinning behavior exhibited by the higher CMC concentration is able to decrease the viscosity more significantly, resulting in the bubble to deform more and more as D_e increases.

Fig. 7 (d) shows the sphericity of the bubble, S. Although various bubble shapes are observed in Fig. 5, both Newtonian and non-Newtonian systems seem to give the same correlation between E and S, which is well approximated by the following Gaussian expression:

$$E(S) = a_1 \exp\left[-\left(\frac{S-b_1}{c_1}\right)^2\right] + a_2 \exp\left[-\left(\frac{S-b_2}{c_2}\right)^2\right] + a_3 \exp\left[-\left(\frac{S-b_3}{c_3}\right)^2\right] \tag{8}$$

where $a_1 = 6.4 \times 10^{12}$, $b_1 = 1.7$, $c_1 = 0.13$, $a_2 = -0.017$, $b_2 = 0.98$, $c_2 = 2.5 \times 10^{-4}$, $a_3 = 1.4 \times 10^{2}$, $b_3 = 3.4$, and $c_3 = 1.1$. The coefficient of determination, $R^2 = 0.9903$, is high enough to indicate Eq. (8) as a good model. The applicability of Eq. (8) to all investigated systems suggests that it is sufficient to measure either the bubble aspect ratio or sphericity to describe the extent of bubble deformation.

3.1.2. Bubble trajectory

Similarly to the results for Newtonian fluids, the same three regimes for the bubble trajectory are found in the non-Newtonian shear-thinning fluid. Fig. 8 shows the different characteristics of rectilinear, helical, and zigzag trajectories. In Fig. 8 (a), the bubble follows a rectilinear path when the size is small enough, i.e., the shear force due to external perturbations is not strong enough to generate a non-symmetric wake and initiate the bubble oscillations (Tagawa et al., 2014). This results in a relatively constant value of v_t, D_e, and E. When the bubble becomes larger, the shear force increases and instabilities appear. In this case, the bubble rises in a helical trajectory where two counter-rotating vorticities are observed (Zenit and Magnaudet, 2009). This condition is indicated by the bubble displacement that deviates from a linear trend, as shown in Fig. 8 (b). While the time evolution of D_e and E oscillates, v_t stays constant for a helical trajectory. Similar trends are observed for the zigzag trajectory, Fig. 8 (c), except for the time evolution of v_t which oscillates due to a periodic vortex generated by the wake of the now larger bubbles. Visual observations on the bubble trajectory in relation with bubble wakes were discussed in Zenit and Magnaudet (2009), De Vries et al. (2002), and Lunde and Perkins (1998).

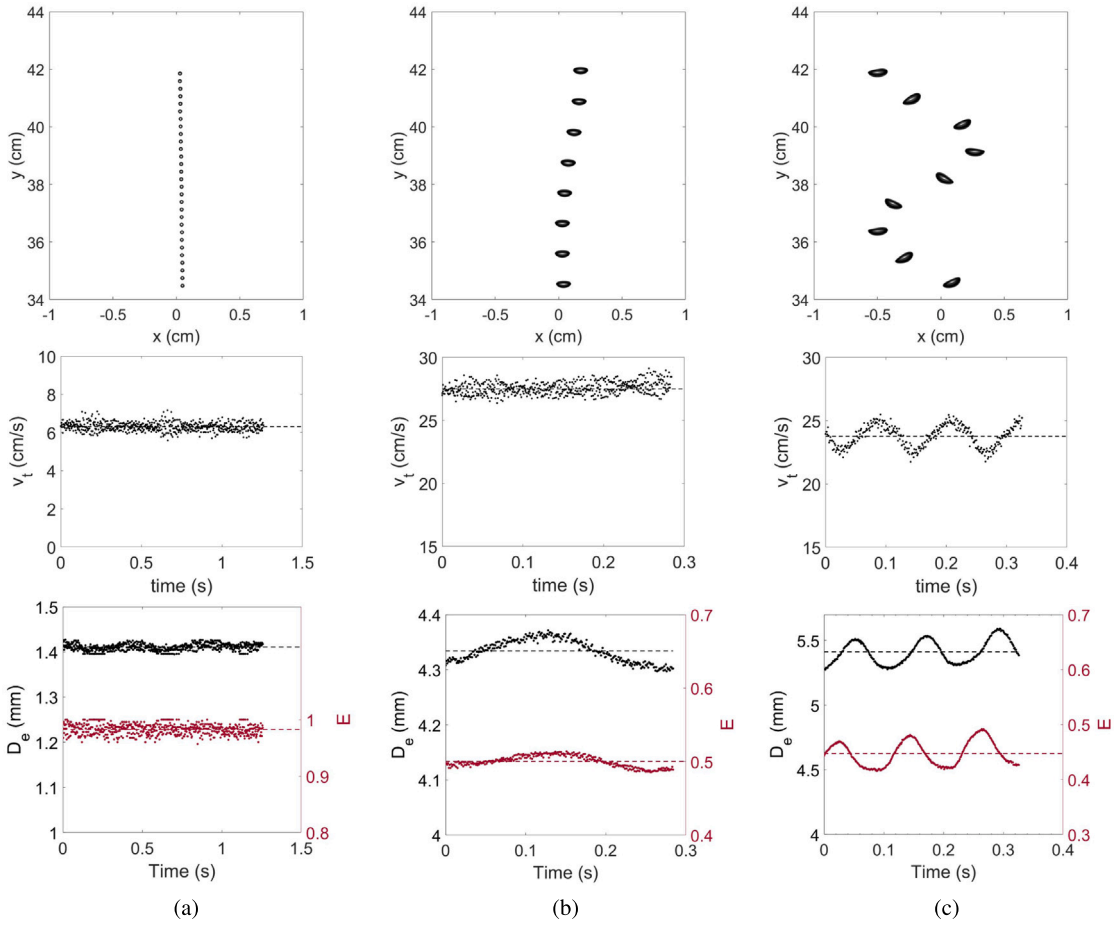

Fig. 8. Time evolution of the bubble displacement, terminal velocity, equivalent diameter, and aspect ratio in CMC 0.05% for (a) rectilinear, (b) helical, and (c) zigzag trajectories, obtained for $D_e = 1.4$ mm, $D_e = 4.3$ mm, and $D_e = 5.4$ mm, respectively. The bubble displacement is visualized with $\Delta t = 400$ ms.

3.1.3. Bubble terminal velocity

Fig. 9 presents the terminal velocity for different bubble sizes in water, which gives a similar trend as described in Fan and Tsuchiya (1990). In this study, it was shown that three different forces: viscosity, surface tension, and inertia dominate the terminal velocity at low, intermediate, and large bubble sizes. As discussed by Clift (1978) and Liu et al. (2016), in the viscous-dominated regime where the bubbles are nearly spherical, the rising velocity is determined by a balance between buoyancy and viscous forces, which lead to an increase of v_t with D_e as presented in Fig. 9 for $D_e \leq 1.37$ mm. When the bubble becomes larger than $D_{e,osc} \approx 1.37 - 1.51$ mm, it begins to oscillate, resulting in the bubble instability under which the surface tension starts to dominate the bubble evolution. This condition results in a greater extent of bubble deformation and trajectory shifting to either helical or zigzag. Since the bubble requires more time to rise in these non-linear trajectories, the terminal velocity becomes slower with bubble sizes, as observed in Fig. 9 for $1.37 \leq D_e \leq 6$ mm. Within the transition regime from linear to non-linear trajectories, a wide scattering of velocity starts to appear. As discussed in Tomiyama et al. (2002) and Wu and Gharib (2002), the scattered velocities in water are caused by the various E values which depend on the ratio of the bubble size to the inner diameter of the needle tip, D_e/D_{cap}. In their analyzes, the high velocities correspond to less spherical bubbles moving in helical trajectory, while the low velocities are obtained for relatively more spherical bubbles having zigzag trajectory. When the bubble becomes even larger, $D_e \geq 6$, the velocity scattering in Fig. 9 narrows to a relatively constant range at $v_t \approx 20 - 25$ cm/s. This indicates that the effect of surface tension reduces and the system begins to shift into the

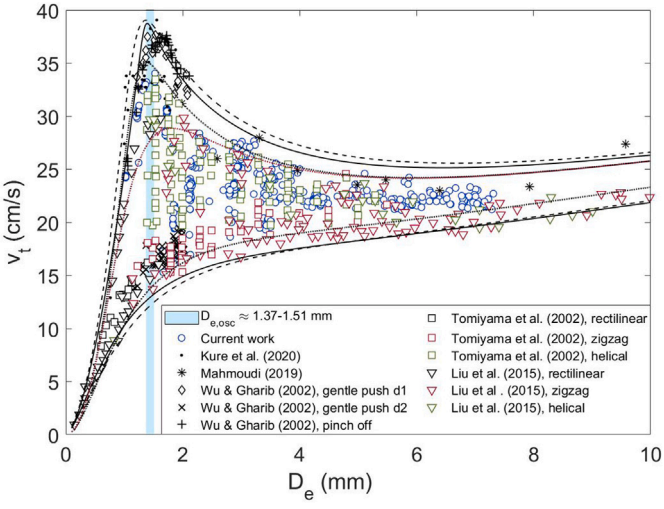

Fig. 9. Terminal velocity as a function of bubble equivalent diameter for water system in comparison to existing experimental data from the literature. All data is obtained as single data points, except for Kure et al. (2021) which represents statistical averaged data points. $D_{e,osc}$ denotes D_e at which the bubble starts to oscillate and the trajectory shifts from rectilinear to helical or zigzag. d_1 and d_2 refer to $D_e/D_{cap} \gg 1$ and $D_e/D_{cap} \approx 1$, respectively. The red dotted-lines represent the original Fan and Tsuchiya (1990)'s model while the black dotted-, dashed-, and solid lines denote the fitted models of Fan and Tsuchiya (1990), Baz-Rodríguez et al. (2012), and Maneri and Vassallo (2000). The corresponding fluid properties and the fitted model parameters are presented in Table A.1. (For interpretation of the references to color in this figure legend, the reader is referred to the web version of this article.)

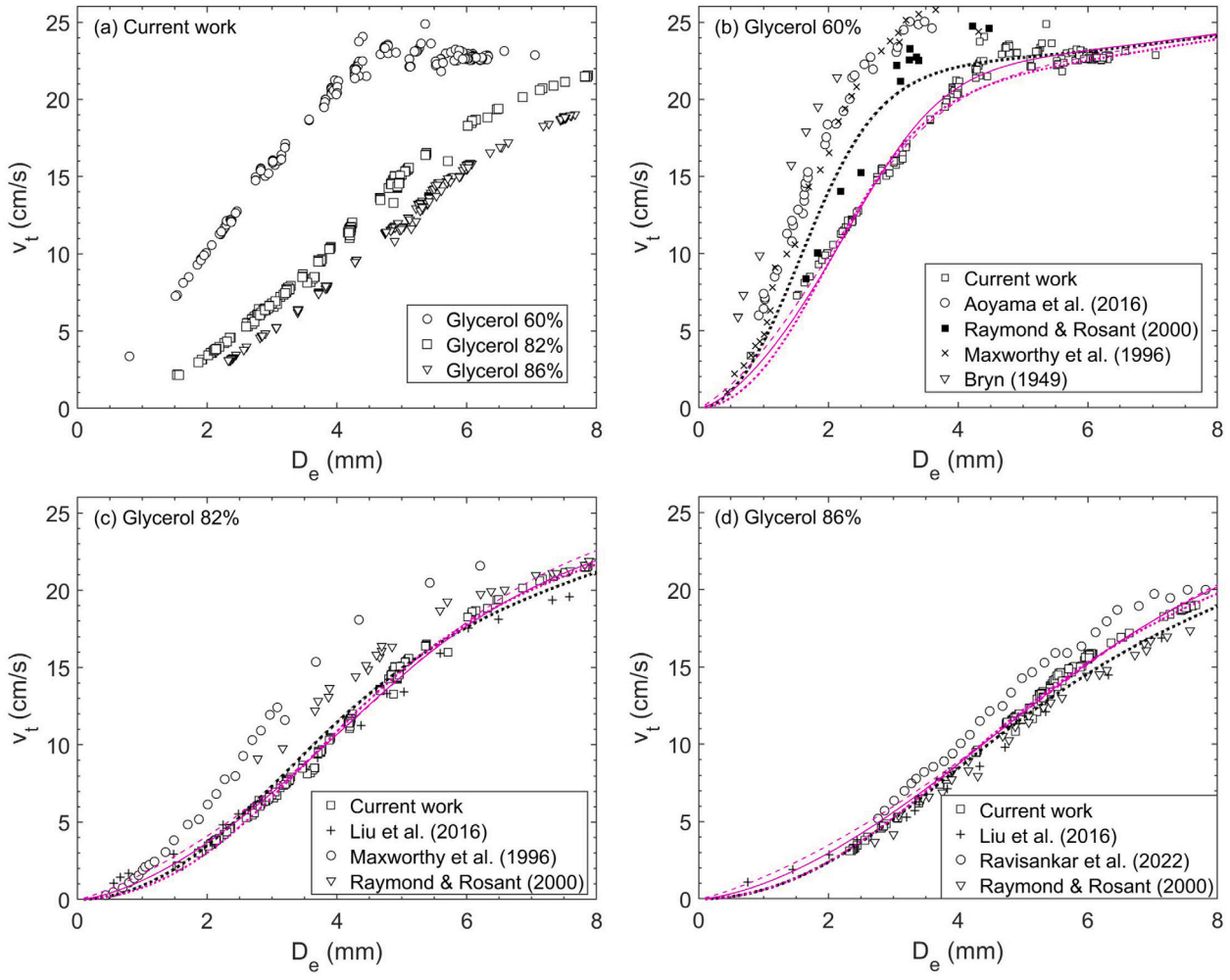

Fig. 10. Terminal velocity as a function of bubble equivalent diameter for (a) glycerol 60%, 82%, 86% and (b)–(d): the comparison of each concentration to existing experimental data from the literature. The black dotted-lines represent the original Fan and Tsuchiya (1990)'s expression while the purple dotted-, dashed-, and solid lines denote the fitted models of Fan and Tsuchiya (1990), Baz-Rodríguez et al. (2012), and Maneri and Vassallo (2000). The corresponding fluid properties and the fitted model parameters are presented in Table A.1 (Appendix A).

inertia-dominated regime. This regime is characterized by increasing v_t with D_e, as shown in Fig. 9 for $D_e \geq 7$ mm in Mahmoudi et al. (2019)'s and Liu et al. (2015)'s results.

3.1.3.1. Effect of bubble deformation and fluid viscosity on the velocity scattering

Fig. 10 shows the terminal velocity for glycerol systems in comparison to the existing literature for comparable physical properties as summarized in Table A.1 (Appendix A). In Fig. 10 (a), all glycerol solutions reveal increasing trend in v_t with D_e, where, for a given D_e, v_t decreases with glycerol concentration. This indicates that the fluid viscosity tends to slow down the bubble due to the stronger flow resistance provided by higher viscosity. As a consequence, the effect of the surface tension dominates the bubble dynamic at a lower D_e for the less viscous system, as indicated by the maximum v_t value for glycerol 60% that reaches $v_{t,max} \approx 25$ cm/s at $D_{e,osc} \approx 5$ mm. Unlike this case, the two most concentrated glycerol solutions only show the viscous-dominated regime where all bubbles show rectilinear trajectory.

Compared to the existing literature, there seems to be a velocity scatter, especially for glycerol 60% as clearly shown in Fig. 10 (b). The extent of the scattering seems to decrease with viscosity, i.e., increasing concentrations of glycerol. This pattern is also observed in Fig. 11 (a) where the bubble deformation is plotted against D_e. The curves for the two most concentrated glycerol solutions fit well with similar systems in the literature. Meanwhile, glycerol 60% appears to give higher E values compared to the existing literature, which, therefore, results in relatively lower velocities. It is also observed in Fig. 10 (b) that the terminal velocity v_t obtained by Raymond and Rosant (2000) has approximately the same values as in the current work for small bubbles. As the bubble becomes larger, Raymond and Rosant (2000)'s results approach those in Aoyama et al. (2016) and Maxworthy et al. (1996). These discrepancies may occur due to some differences in the experimental setup, e.g., the design of the needle tip, D_e/D_{cap}, injection method, injection rate, or the different method of estimating the bubble properties, due to different image resolution, image threshold estimation, or D_e computation method. When the viscosity increases with glycerol concentrations, the velocity scatter decreases as shown in Figs. 10 (b)–(d). Although the systems have the Morton number, $Mo = \frac{g\mu^4(\rho_l-\rho_g)}{\sigma^3\rho_l^2}$, in the same order of magnitude, as summarized in Table A.1 (Appendix A), the specific value of Mo appears to have a more pronounced impact on v_t as its magnitude decreases. Fig. 11 (b) shows that $Mo \approx 4 \times 10^{-3}$, which corresponds to Glycerol 86%, seems

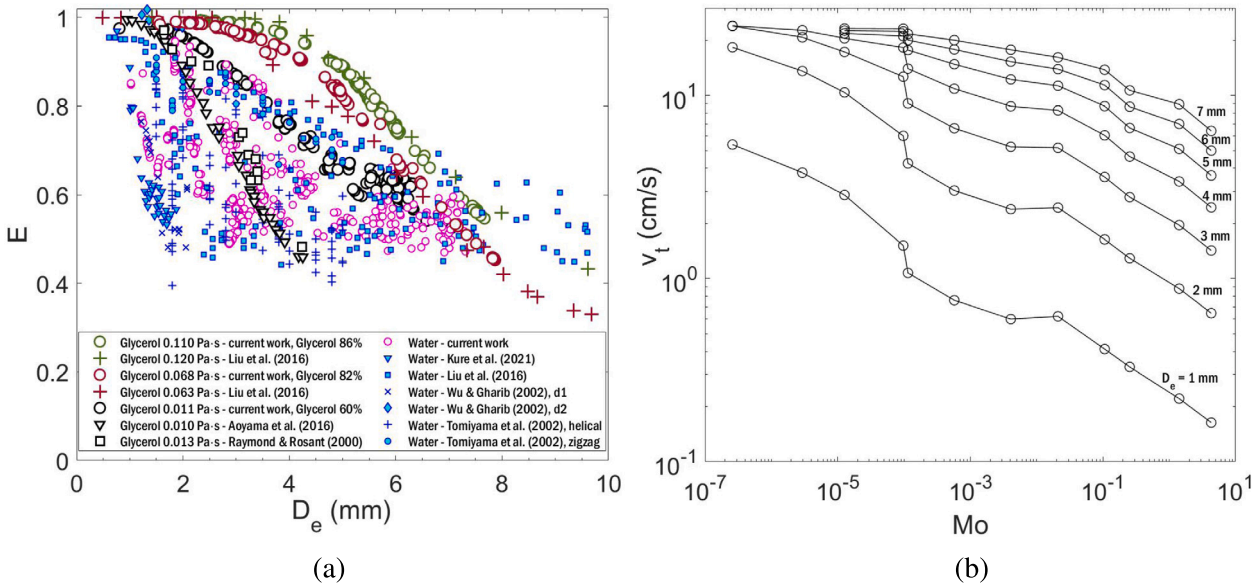

Fig. 11. (a) Bubble aspect ratio as a function of bubble diameter for Newtonian systems and (b) terminal velocity as a function of the Morton number for various bubble sizes. All data is obtained as single data points, except for Kure et al. (2021) which represents statistical averaged data points. d_1 and d_2 refer to $D_e/D_{cap} \gg 1$ and $D_e/D_{cap} \approx 1$, respectively.

to be the critical value determining the effect of different Mo on v_t. Below this value, the gradient of v_t/Mo increases with decreasing Mo, indicating that v_t becomes more sensitive with decreasing Mo.

The applicability of the original Fan and Tsuchiya (1990)'s model, marked as the black dotted-lines in Fig. 10, is compared with the Baz-Rodríguez et al. (2012)'s and Maneri and Vassallo (2000)'s models which are fitted to the experimental results. Based on the model parameter values obtained in this study, the expression of Maneri and Vassallo (2000) can be generalized by changing the constant parameter K to a function of the Morton number, Mo, resulting in a logarithmic correlation: $K = 6.7[-log(Mo)^{1.3}]$. Fig. 16 (a) presents the agreement of the modified Maneri and Vassallo (2000)'s model with the experimental data.

3.1.3.2. *Effect of the shear-thinning*

The terminal velocity for non-Newtonian fluids is compared with the existing experimental data in the literature as shown in Fig. 13 (a). The comparable velocities between the current study and the literature data in Fig. 12 (a) indicate that the systems studied here have similar rheology conditions, i.e., apparent viscosity and shear rates, as the ones in the literature. Here, the apparent viscosity refers to the resistance of a fluid to flow under applied shear. Based on Fig. 13, the shear rate is estimated to lie between $\dot{\gamma} = 5 - 210\ \mathrm{s}^{-1}$ where the lower shear rates, which correspond to the higher viscosities, are exhibited by the higher CMC concentration. Since higher CMC concentrations give higher μ_0, it is relatively easier for these fluids to resist the shear rate generated by the bubble movement. As the result, v_t obtained for higher CMC concentrations is lower than the ones for lower CMC concentrations, as shown in Fig. 12 (a). This effect holds within the viscous-dominated regime until the trajectory shifts from linear to helical at which v_t reaches its highest point. The peak values of v_t seem to decrease with CMC concentrations, reaching $v_{t,max} = 28$ cm/s, $v_{t,max} = 26$ cm/s, and $v_{t,max} = 24$ cm/s for CMC 0.05%, CMC 0.10%, and CMC 0.20%, respectively. These values are obtained at a larger $D_{e,osc}$ for more concentrated CMC which indicates that higher CMC concentration tends to enlarge the range of D_e where the viscous-dominated regime occurs. When v_t for CMC 0.05% starts to decrease at $D_e \approx 4$ mm, the bubble trajectory was observed to switch to helical. For the same D_e, the bubbles in CMC 0.10% and CMC 0.20% were observed to rise in rectilinear trajectory which is also indicated by the increasing trend of v_t with D_e. This implies that shear-thinning behavior tend to decrease

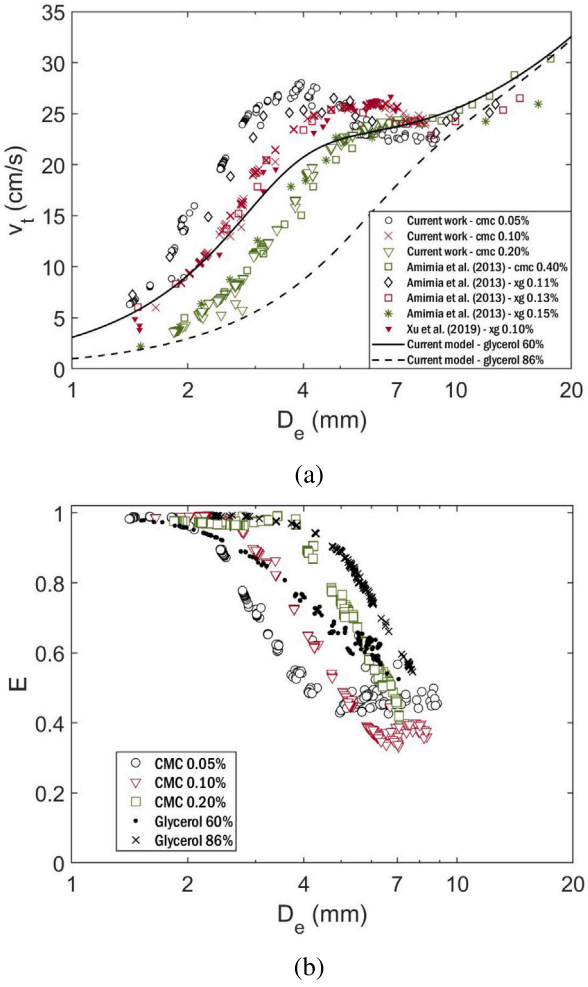

Fig. 12. (a) Terminal velocity and (b) aspect ratio of the rising bubbles as a function of equivalent diameter for different fluids.

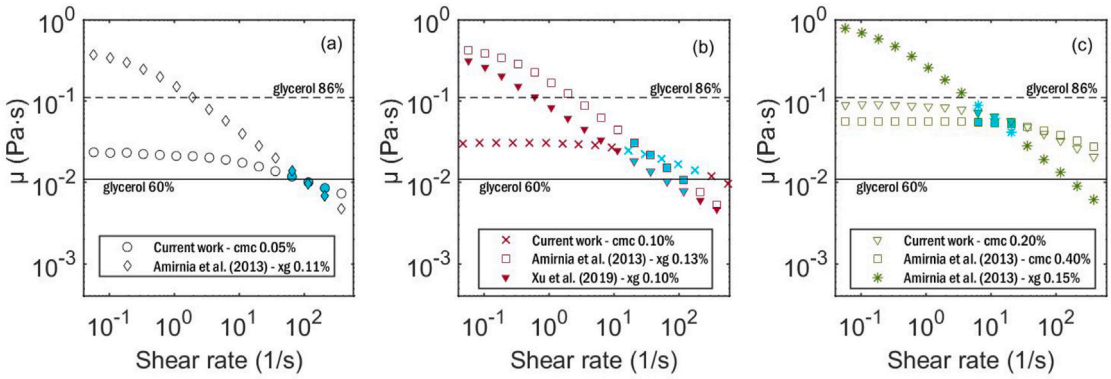

Fig. 13. Rheology for (a) CMC 0.05%, (b) CMC 0.10%, and (c) CMC 0.20%. The cyan color represents similar viscosities under the same shear rates. (For interpretation of the references to color in this figure legend, the reader is referred to the web version of this article.)

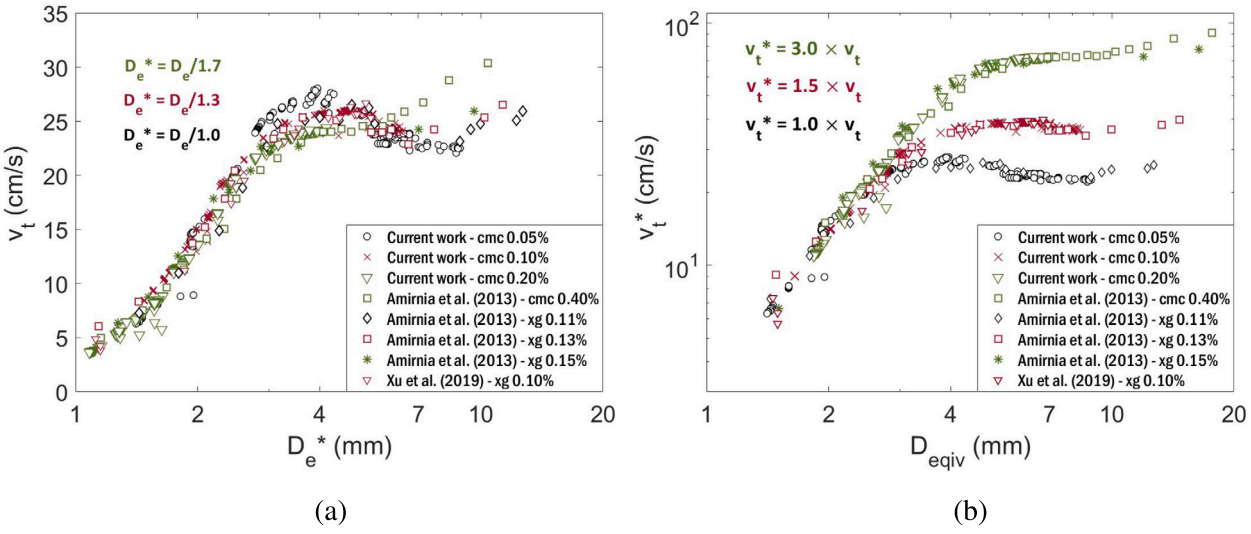

Fig. 14. The shifted plots of Fig. 12 with (a) modified equivalent diameter, D_e^* and (b) modified terminal velocity, v_t^*. All results are plotted with comparable velocities in the existing literature.

the horizontal motion of small bubbles, which is consistent with Hassan et al. (2008)'s analysis. The values of $D_{e,osc}$ seem to coincide with D_e at which E reaches a constant value, hereby denoted as E_{fin}, revealing another indicator of the regime transition from viscous- to surface-tension-dominated regime. Since the regime transition for the three cases occurs at different $D_{e,osc}$, the effect of shear-thinning parameters in the surface-tension-dominated regime is analyzed by shifting the curves.

Figs. 14 (a) and 14 (b) are obtained by dividing D_e and multiplying v_t with a coefficient to yield a modified equivalent diameter, D_e^*, and a modified velocity, v_t^*. It is seen from Fig. 14 (a) that v_t decreases with higher CMC concentration, i.e. higher μ_0 and lower E_{fin}, under the surface-tension-dominated regime that occur between $D_e^* = 3-5.7$ mm. The effect of μ_0 on decreasing v_t seems to be consistent with the analysis in the viscous-dominated regime. Meanwhile, the contribution of E to increasing v_t, as discussed in Tomiyama et al. (2002) and Wu and Gharib (2002) for Newtonian systems, seems to be less prominent compared to the effect of μ_0 in this regime.

In the inertia-dominated regime, shear thinning has an opposite effect: higher CMC concentrations result in higher v_t values. Notice that although D_e^* for CMC 0.20% hardly reaches the inertia-dominated regime, the comparable systems obtained in Amirnia et al. (2013) seem to show a consistent effect. This effect looks more visible in Fig. 14 (b) where the upper curves are obtained for higher CMC concentrations. Unlike the Newtonian cases where viscosity is negligible in the inertia-dominated regime, the decreasing viscosity, i.e., due to shear-thinning behavior, in non-Newtonian fluids seems to influence the terminal velocity by increasing the extent of bubble deformation, i.e., decreasing the aspect ratio. As shown in Fig. 12 (b), E for CMC 0.10% decreases to a lower value than the ones for 0.05% which seem constant at $E_{fin} \approx 0.4$. This indicates that the shear-thinning effect on decreasing the aspect ratio, i.e., effect of the power-law index p on decreasing E, becomes more influential in the inertia-dominated regime. By re-visiting the deformation effect discussed in Section 3.1.3.1, the same relationship also holds here, where lower E obtained in higher CMC concentration tends to result in higher v_t under the inertia-dominated regime as indicated in Fig. 14 (b).

Compared to the Newtonian cases, the three CMC solutions in Fig. 12 (a) give a higher gradient of v_t/D_e. The curve for CMC 0.20% indicates similar terminal velocities as the ones for glycerol 86% when $D_e \leq 1.5$ mm. The shear-thinning effect starts to appear and becomes more pronounced for larger bubbles, $D_e > 1.5$ mm, when the curve for CMC 0.20% in Fig. 12 deviates from glycerol 86% and approaches glycerol 60% at around $D_e \approx 5.1$ mm. In this condition, bubbles rising in glycerol 86% and CMC 0.20% are within the viscous-dominated regime, while the flow in the glycerol 60% solution is no longer dominated

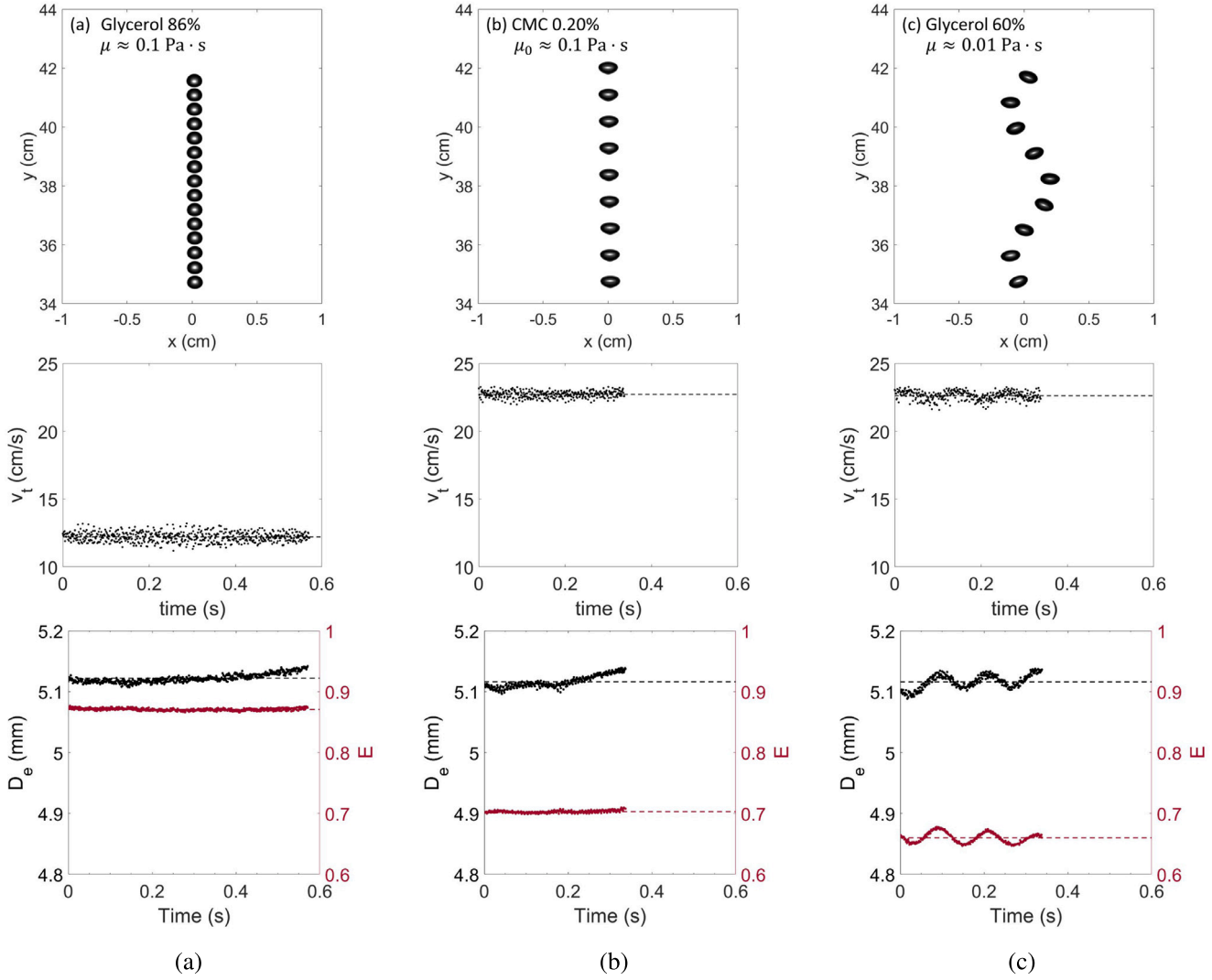

Fig. 15. Time evolution of bubble displacement, terminal velocity, equivalent diameter, and aspect ratio for 5.12 mm bubble in (a) Glycerol 86%, (b) CMC 0.20%, and (c) Glycerol 60%. The bubble displacement is visualized with Δt = 40 ms.

by the viscosity, as observed in Fig. 15. Although both glycerol 60% and CMC 0.20% cases show the same averaged values of v_t and D_e, the bubbles rise with a different trajectory for different E values, indicating that the shear-thinning changes not only the viscosity but also the bubble deformation. Therefore, both shear-dependant viscosity and aspect ratio need to be considered to estimate the terminal velocity in non-Newtonian systems.

The shear-thinning effects are initially investigated by comparing results for shear-thinning liquids with the ones for Newtonian fluids having the same viscosity as the zero shear-rate viscosity. In this respect, CMC 0.2% and glycerol 86% are taken as the reference cases having equal zero-shear viscosity ≈ 0.1 Pa s, as indicated in Fig. 13 (c). Fig. 12 (a) shows that for small bubbles, i.e., $D_e \leq 1.5$ mm, both cases give similar terminal velocities, suggesting minimal shear-thinning effects. In this case, the viscosity of CMC 0.20% is expected to be the same as the zero-shear viscosity. By assuming effective shear rate, i.e., $\dot{\gamma}_{\text{eff}} = v_t/(D_e/2)$ or $\dot{\gamma}_{\text{eff}} = v_t/D_e$, the effective viscosity for the bubble properties, $D_e \approx 1.5$ mm and $v_t \approx 2.2$ cm/s, is calculated to be $\mu_{\text{eff}} \approx 0.05$ Pa s, which is half of the zero-shear viscosity. This discrepancy is further analyzed by evaluating the terminal velocity expressions of Fan and Tsuchiya (1990), Maneri and Vassallo (2000), Baz-Rodríguez et al. (2012), and Rodrigue (2002), given in Table 1. It is found that applying this assumption lead to poor fit in the velocity expressions, indicating that there may be some unaccounted effects of shear-thinning viscosity that need to be empirically considered in the existing semi-empirical models of terminal velocity. Therefore, the viscosity estimation is adjusted to minimize the standard error of the fitted terminal velocity, resulting in a quadratic relationship:

$$\mu_l(D_e) = x_1 D_e^2 + x_2 D_e + x_3 \tag{9}$$

where $x_1 \in 4\times10^{-5}, 9\times10^{-5}, 4\times10^{-4}$, $x_2 \in -2\times10^{-4}, -6\times10^{-4}, -4\times10^{-3}$, and $x_3 \in 4.1\times10^{-3}, 7.7\times10^{-3}, 2.4\times10^{-2}$ are the fitting parameters. Eq. (9) is later found to coincide with the simulation results provided in Section 3.2, assuming the average viscosity near the bubble interface. Considering that the aspect ratio is influential for the intermediate-to-large bubbles, which is represented by v_{b2}, the Maneri and Vassallo (2000)'s expression is modified by adapting Tomiyama et al. (2002)'s expression to yield the expression in Table B.1 (Appendix B). Fig. 16 (a) shows good agreement of the modified Maneri and Vassallo (2000)'s expression, where a high value of the coefficient of determination, $R^2 = 0.9883$, is obtained for the CMC cases. The model fitting was also performed for $\dot{\gamma}_{\text{eff}} = v_t/D_e$, indicating Fan and Tsuchiya (1990)'s expression as the best model. Fig. 16 (b) shows the accuracy of the modified Fan and Tsuchiya (1990)'s expression.

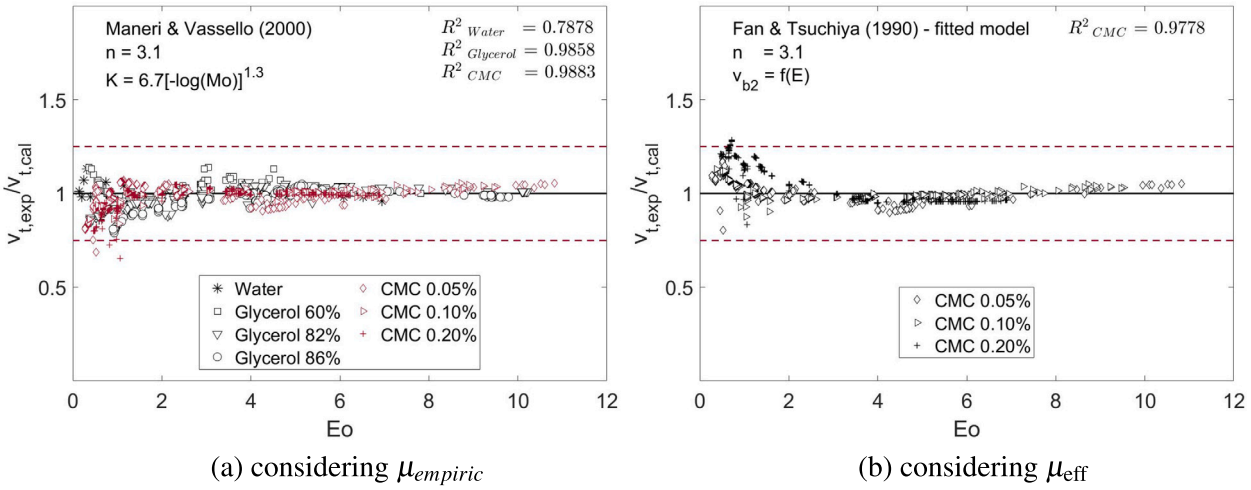

Fig. 16. The ratio of experimental to calculated velocities as a function of Eötvös number, $Eo = \frac{(\rho_l - \rho_g) g D_e^2}{\sigma}$, for (a) different Newtonian and non-Newtonian systems considering Eq. (9) and (b) different CMC solutions assuming μ_{eff}. The red dashed-lines represent ±25% of the true value. R^2 is the coefficient of determination which represents the quality of the approximation. Additional details on the fitted models are given in Appendix B.

3.2. Simulation results

The numerical simulations were performed for small and large bubbles in 6 different systems as summarized in Table 4. Case (a) represents the most extreme cases with $D_e = 1.41$ mm and $D_e = 8.88$ mm as the smallest and the largest bubbles obtained in the experiment. Case (e) refers to the experimental system of Amirnia et al. (2013) which exhibits similar v_t values as CMC 0.10%. This case is examined to understand the shear-thinning behavior for lower p, i.e., stronger shear-thinning than the CMC solutions in the current work.

Table 4
Numerical simulation cases.

Case	Fluid	D_e (mm)	
		Small size	Large size
(a)	CMC 0.05 wt% in water	1.41	8.88
(b)	CMC 0.05 wt% in water	2.00	7.00
(c)	CMC 0.10 wt% in water	2.00	7.00
(d)	CMC 0.20 wt% in water	2.00	7.00
(e)[a]	XG 0.13 wt% in water	2.00	7.00
(f)	Glycerol 60 wt% in water	2.00	7.00

[a] Amirnia et al. (2013).

3.2.1. Comparison between simulation and experiment

Figs. 17 (a)–(c) show the comparison between simulation and experimental results for CMC 0.05% with three different bubble sizes. For small bubbles in Figs. 17 (a)–(b), the simulation shows increasing vertical velocity until it reaches its terminal state after $t \approx 0.05$ s. We observe approximately the same deviation, $\Delta v_t = 14.4\%$ and $\Delta v_t = 13.3\%$, for $D_e = 1.41$ mm and $D_e = 2$ mm. This indicates that the estimation is less sensitive to the change in D_e when the bubble is small enough. Fig. 17 (d) presents the comparison for the other studied cases mentioned in Table 4. Unlike the non-Newtonian cases where the deviation lies below 25%, Δv_t for glycerol 60% reaches 34.5%. The large deviation in v_t may arise due to differences in the initial bubble deformation between simulations and experiments. In the simulation, the bubble is assumed to be initially spherical. This assumption does not always hold in the experiment, where the initial bubble shape depends on the injection setup, as discussed in Section 3.1.3.1. Nevertheless, the simulation result seems to follow the Fan and Tsuchiya (1990)'s model, provided in Table 1, giving a deviation of only $\Delta v_t = 8.1\%$. This argument seems consistent for the other bubble sizes where v_t obtained from the simulation follows the Fan and Tsuchiya (1990)'s model rather than the experimental results of the current work or the existing literature. As the bubble size increases, Δv_t becomes smaller and eventually reaches 2.8% for $D_e = 7$ mm. Appendix D provides more details on the comparison with the simulations for the different cases under consideration.

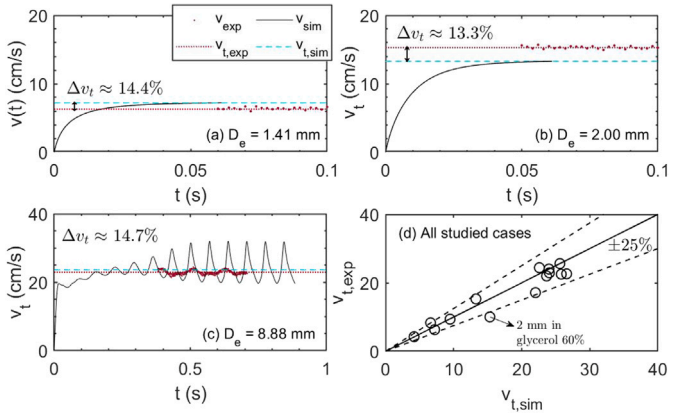

Fig. 17. (a)–(c) Vertical velocity obtained for different D_e in CMC 0.05% and (d) experimental vs simulation results for the different cases in Table 4. Symbols in (a)–(c) are defined as solid line: simulation, dashed-line: terminal velocity estimated from simulation, dots: experiment, dotted-line: terminal velocity estimated from experiment.

3.2.2. Viscosity field of non-Newtonian media

Fig. 18 shows the time-dependent viscosity field around a single 8.88 mm bubble in CMC 0.05%. Although the initial shape is assumed to be spherical, the bubble deforms already at $t = 0.03$ s, where a viscosity blind area, defined as an area having similar viscosity as the zero-shear-viscosity (Pang and Lu, 2018), occurs below the bubble. As the velocity increases with time, the viscosity blind area becomes wider, giving a rim-like-shape in the viscosity field under the bubble.

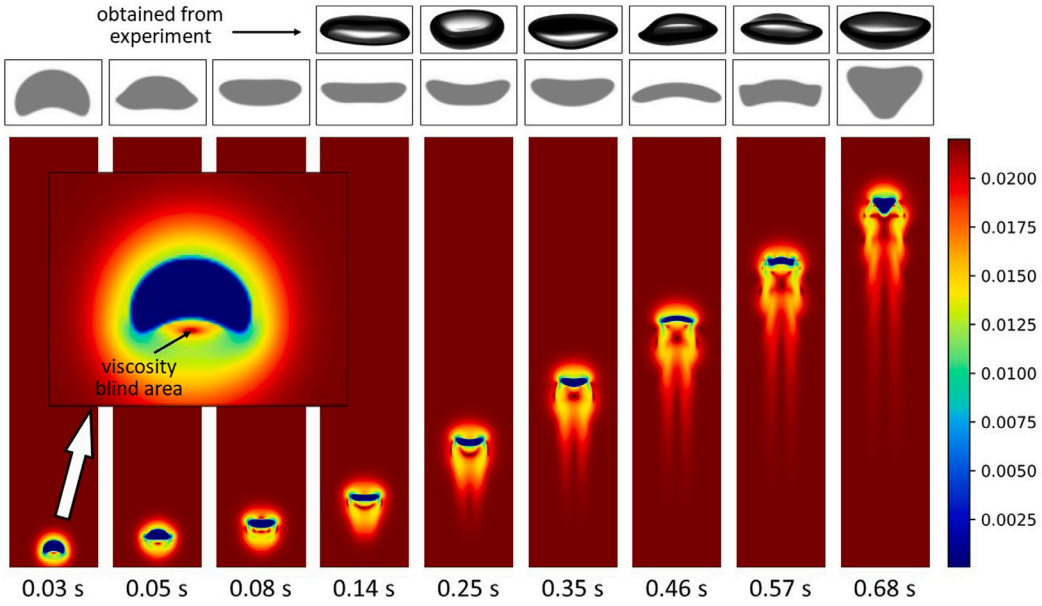

Fig. 18. Time evolution of viscosity field (Pa s) for 8.88 mm bubble in CMC 0.05%. The bubble shapes in the first and the second rows are obtained from experiments and simulations, respectively.

This area becomes less visible when CMC concentrations increase, as shown in Fig. 19, where the shear-thinning-affected area becomes more extensive. The viscosity blind area completely disappears in XG case, the right-most figure, where the shear-thinning behavior is even more pronounced than the one for the CMC cases. Unlike the deformed bubbles, the viscosity blind area is not observable for small bubble cases as presented in Fig. 20 where the bubble stays spherical. In these cases, the greatest effect of shear-thinning behavior occurs in the top and the bottom of the bubble, indicating that the shear forces within these domains are higher than those on the side of the bubbles. These two regions become more evident for larger CMC concentrations. Compared to the CMC cases, the shear-thinning behavior exhibited in XG seems more pronounced as shown in the right-most picture of Figs. 19–20, where the affected domain is the widest among the four cases.

3.2.3. Apparent viscosity for terminal velocity modeling

Figs. 21 (a)–(c) show the apparent viscosity estimated by three approaches: the common assumption of effective shear rate $\dot{\gamma}_{\text{eff}} = v_t/D_e$, the empirical method as expressed in Eq. (9), and the average viscosity computed from the viscosity field. Hereafter, the three viscosities are denoted as μ_{eff}, $\mu_{empiric}$, and μ_{sim}. The computed μ_{sim} is obtained for 2 different domains having diameters of $D_{dom} = 1.02D_e$ and $D_{dom} = 2D_e$. When $D_{dom} = 2D_e$, the μ_{sim} values coincide with μ_{eff}. This, however, does not apply for 7 mm bubble in XG 0.13%. Meanwhile, μ_{sim} seems to fit well with $\mu_{empiric}$ when the domain outside the bubble interface is limited to only 2% of D_e, i.e., $D_{dom} = 1.02D_e$. This may indicate that the domain where the viscosity influences the bubble velocity is limited to the proximity of the bubble interface. Fig. 21 (d) displays μ_{sim} computed for different averaging domains, with a range of $D_{dom} = 1.02D_e - 20D_e$. It is shown that μ_{sim} decreases with decreasing D_{dom}. The computed μ_{eff} appears on various D_{dom}/D_e, ranging between $D_{dom}/D_e \approx 1.1 - 2.2$. As D_{dom} gets closer to D_e, i.e., $D_{dom}/D_e < 1.15$, μ_{sim} decreases with a steeper slope, and eventually reaches $\mu_{empiric}$. The curves for $D_e = 2$ mm and $D_e = 7$ mm become more distinguishable when the shear-thinning effect is stronger, i.e., p is lower. Nevertheless, the effect of D_{dom} on the viscosity change seems to be greater than the effect of D_e.

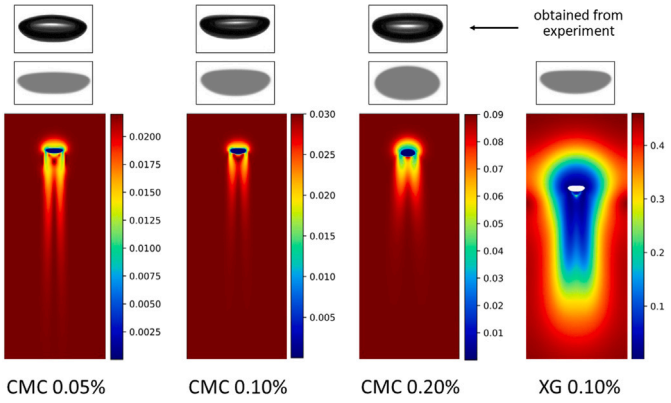

Fig. 19. Viscosity field (Pa s) for 7 mm bubble in CMC 0.05%, CMC 0.10%, CMC 0.20%, XG 0.13% obtained at steady state. The bubble shapes in the first and the second rows are obtained from experiments and simulations, respectively. The bubble for XG 0.13% case is recolored into white to distinguish it from the blue zone of the viscosity field.

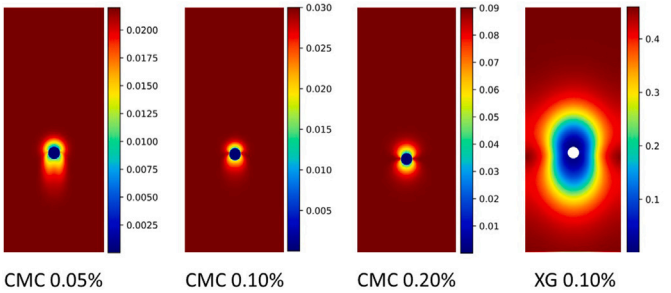

Fig. 20. Viscosity field (Pa s) for 2 mm bubble in CMC 0.05%, CMC 0.10%, CMC 0.20%, XG 0.13% obtained at steady state. The bubble for XG 0.13% case is recolored into white to distinguish it from the blue zone of the viscosity field.

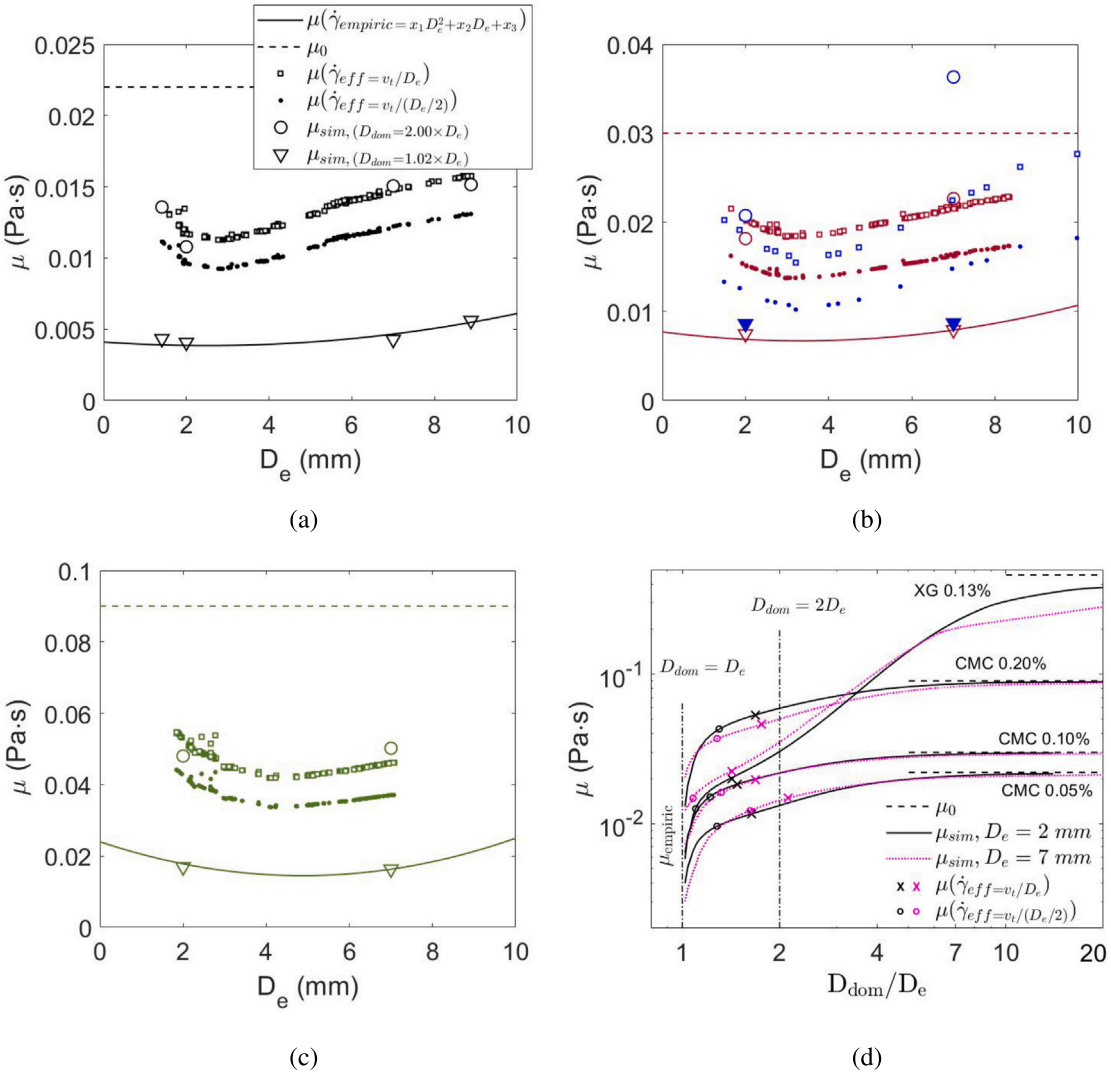

Fig. 21. Viscosity estimation for (a) CMC 0.05%, (b) CMC 0.10% in comparison to Amirnia et al. (2013)'s XG 0.13% (marked in blue), (c) CMC 0.20%, and (d) average viscosity as a function of specified domain, D_{dom}/D_e, where the solid and the dot-dashed lines are obtained for $D_e = 2$ mm and $D_e = 7$ mm, respectively. (For interpretation of the references to color in this figure legend, the reader is referred to the web version of this article.)

3.3. Drag coefficient

The effect of fluid shear-thinning is investigated further for drag coefficient, C_D. The common expression of C_D for a spherical body is obtained from the force balance between buoyancy and drag forces in the terminal state, which yields a drag correlation as Eq. (10). For deformable bubbles, the effect of the bubble aspect ratio has been included in the literature (Wenyuan et al., 2010; Hassan et al., 2008; Islam et al., 2020), in terms of the major axis length, D_{max}, and can be reformulated in terms of E as Eq. (11). Both expressions were evaluated for non-Newtonian systems by Hassan et al. (2008) and Li et al. (2012) using a power law model to estimate the viscosity. Hassan et al. (2008) used Eqs. (10)–(11) where one of their XG systems seems to agree with Dewsbury et al. (1999)'s expression, Eq. (14). The same approach was followed by Zhang et al. (2008a) and yields Eq. (15). Li et al. (2012) examined Eq. (10) by including E and p in a fitted parameter, ψ, resulting in Eqs. (12)–(13). Their expression seems to fit Clift and Gauvin (1971)'s model for Newtonian fluids, Eq. (16). Table 5 summarizes different C_D expressions. The term Re_n refers to the Reynolds number for power law fluids (Clift and Gauvin, 1971; Dewsbury et al., 1999; Zhang et al., 2008a; Hassan et al., 2008), which is expressed as a function of the flow consistency, k, and p.

Table 5
Drag coefficient expressions.

C_D from force balance	
Spherical shape	
$C_D = \frac{4}{3}\frac{gD_b}{v_t^2}\frac{\Delta\rho}{\rho_L}$	(10)
Deformable shape	
$C_D = \frac{4}{3}\frac{gD_b}{v_t^2}\frac{\Delta\rho}{\rho_L}E^{2/3}$	(11)
Deformable shape in power-law fluids (Li et al., 2012)	
$C_D = \frac{4}{3}\frac{gD_b}{v_t^2}\frac{\Delta\rho}{\rho_L}\psi$	(12)
$\psi = 1 + 3.868p^{0.7528}(1-E)^{0.681}$	(13)
In terms of dimensionless, $C_D(Re_n)$	
Dewsbury et al. (1999)	
$C_D(Re_n) = \frac{16}{Re_n}(1+0.173(Re_n)^{0.657}) + \frac{0.413}{1+16300(Re_n)^{-1.09}}$	(14)
Zhang et al. (2008a)	
$C_D(Re_n) = \frac{16}{Re_n}(1+0.12(Re_n)^{0.66})(1+0.196A_c^{0.767}A_r^{0.381})$	(15)
Clift and Gauvin (1971) modified by Li et al. (2012)	
$C_D(Re_n) = \frac{16}{Re_n}(1+0.43(Re_n)^{0.44})\psi$	(16)

Re_n is the Reynolds number for power-law fluids which are written in Dewsbury et al. (1999), Zhang et al. (2008a) and Li et al. (2012).

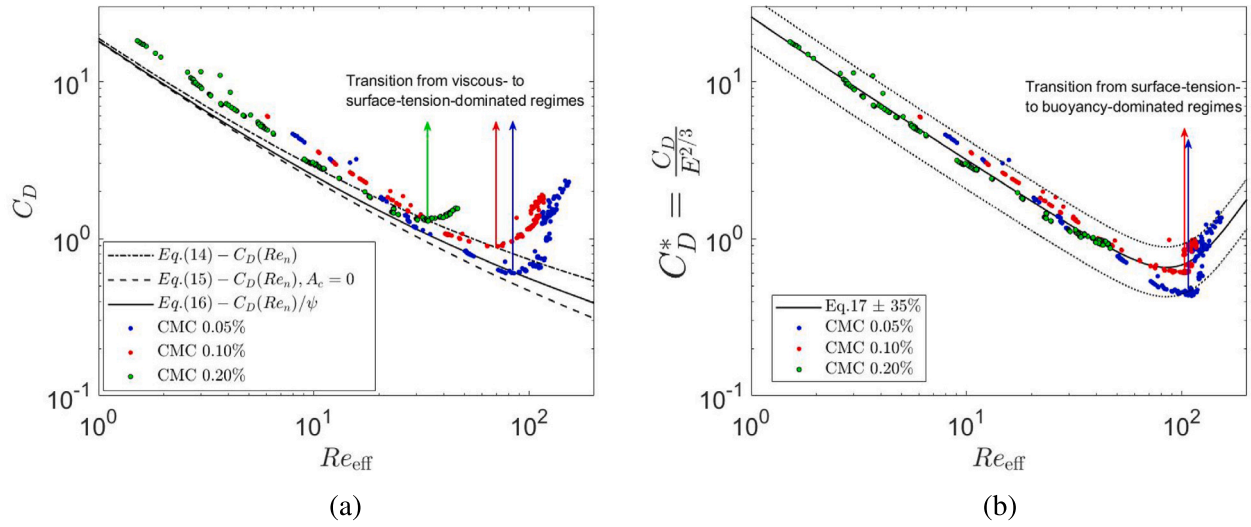

Fig. 22. Experimental drag coefficient obtained from (a) Eq. (10) and (b) Eq. (11) as a function of the effective Reynolds number.

Eqs. (10)–(12) are evaluated for the experimental data by adjusting the Reynolds number to comply with the Carreau model used in this study. The effective shear-rate, $\dot{\gamma}_{\text{eff}} = \frac{v_t}{D_e/2}$, is taken as the reference to find the effective viscosity, μ_{eff}, used for computing the effective Reynolds number, Re_{eff}. Fig. 22 (a) presents the experimental drag coefficient, C_D, obtained from Eq. (10). Unlike the existing models in Eqs. (14)–(16) where C_D monotonously decreases with Re, the three curves for the experimental C_D exhibit a non-monotonic trend where the critical Re_{eff} increases with decreasing CMC concentrations. These critical Re_{eff} are found to coincide with the bubble sizes at which the surface tension forces start to dominate the flow. The critical Re_{eff} shifts when E is included to C_D according to Eq. (11). As observed in Fig. 22 (b), the curves for CMC 0.05% and CMC 0.10% start to increase at $Re_{\text{eff}} \approx 100$ where the corresponding bubble sizes indicate a transition from the surface-tension- to the inertial-dominated regimes. On the other hand, the curve for CMC 0.20% remains decreasing, indicating that the flow has not reached the inertial-dominated regime. Fitting the data with Eq. (14) yields:

$$C_D(Re_{\text{eff}}) = \left[\frac{21}{Re_{\text{eff}}}(1 + 0.223\, Re^{0.355}) + \frac{5.605}{1 + 3.87 \cdot 10^7 Re_{\text{eff}}^{-3.11}}\right] E^{2/3} \quad (17)$$

A new fitting of the data in Fig. 22 (a) in terms of Eo, Mo, and the Archimedes number, $Ar = \frac{g D_e^3 \rho_l (\rho_l - \rho_g)}{\mu^2}$, results in the following empirical expression:

$$C_D = \frac{4.4}{Re^{1.42}}(1 + 0.196 Ar^{0.381})(1 + Eo)^{0.78} Mo^{-0.15} \quad (18)$$

Notice that the term $(1 + 0.196 Ar^{0.381})$ follows the expression of Zhang et al. (2008a) reported in Eq. (15) in Table 5.

Fig. 23 shows the accuracy of μ_{eff} compared to the shear-thinning viscosity near the bubble interface. In the top figures, a discrepancy in C_D is observed for CMC 0.10%, Fig. 23 (a), that is expected to be the same as Amirnia et al. (2013)'s XG 0.13%, as proven by the same terminal velocity curves in Fig. 12. This alignment, however, does not hold for C_D when μ_{eff} is considered, exhibiting up to 50% error. On the other hand, when considering viscosity near the bubble interface, the two curves in Fig. 23 (b) almost collapse. In the bottom figures, the modified expression of C_D^* in Fig. 23 (a) exhibits good agreement between Eq. (18) with the experimental results for both Newtonian and non-Newtonian cases. The accuracy is, however, 10% lower than Fig. 23 (b) when considering the shear-thinning viscosity near the bubble interface.

4. Conclusion

The evolution of a single air bubble rising in Newtonian and non-Newtonian liquids is experimentally and numerically investigated in this work. The bubble equivalent diameter appears to affect the terminal velocity in different ways, depending on the dominant forces between viscous, surface tension, and inertia. In the viscous-dominated regime, i.e., small bubble sizes, the bubble rises in a linear trajectory and the terminal velocity increases with the bubble equivalent diameter. The surface-tension-dominated regime, i.e., intermediate bubble sizes, is indicated by the trajectory shifting from linear to helical or zigzag. In this regime, the terminal velocity for a specific bubble equivalent diameter varies, depending on the initial bubble deformation and the viscosity. The variation in terminal velocity is reduced with viscosity and bubble size. The transition from the surface-tension- to the inertia-dominated regimes is denoted by the increasing terminal velocity with bubble size. In both surface-tension- and inertia-dominated regimes, the bubble aspect ratio is relatively constant.

In shear-thinning fluids, the terminal velocity varies because of the decreasing viscosity and the greater bubble deformation. While the decreasing viscosity is seen to directly change the terminal velocity for small bubbles under the viscous-dominated regime, there seems to be indirect effects for large bubbles where the decreasing viscosity leads to a greater bubble deformation. This results in a reduction of drag and eventually increases the bubble terminal velocity, as also concluded by Rodrigue et al. (1999). The characteristics of the three forces are summarized in Table 6 along with the effects of different rheology parameters and bubble deformation on the bubble terminal velocity.

The experimental and simulation results show good agreement with more deviation obtained for less viscous systems, lower p and μ_0, due to the different initial bubble deformation. Both techniques indicate that the effective shear rate, $\dot{\gamma}_{\text{eff}} = v_t / D_e$, is less accurate compared to considering the shear-thinning viscosity near the bubble interface. Nevertheless, further evaluation for other non-Newtonian fluids is required to obtain a general expression for shear-thinning viscosity near the bubble interface. Finally, the proposed empirical expressions suggest the inclusion of power-law index and bubble deformation to predict the terminal velocity and the drag coefficient more accurately.

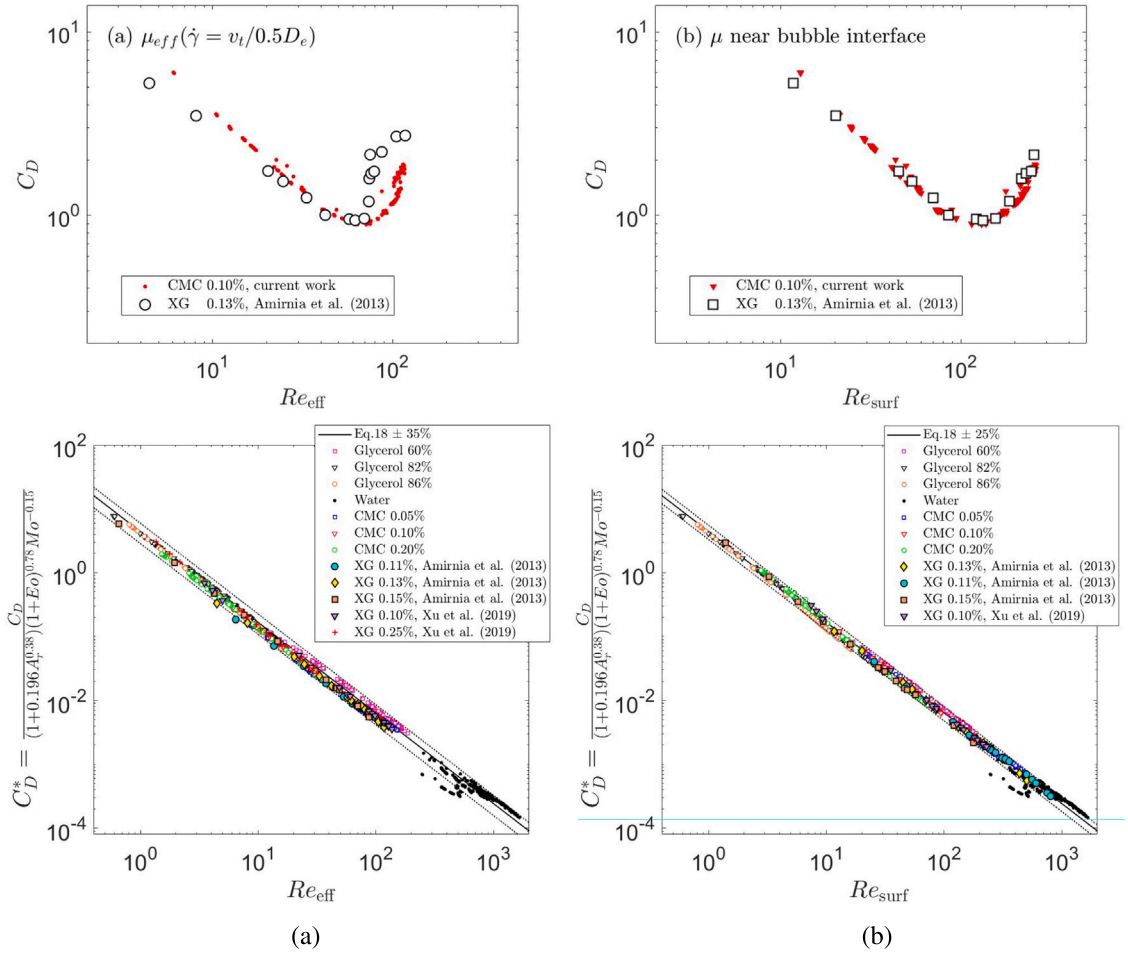

Fig. 23. Experimental drag coefficient obtained from Eq. (10) and the fitted models for drag coefficient as a function of Reynolds number considering (a) effective shear rate and (b) shear rate near the bubble interface.

Table 6
The characteristic of viscosity-, surface-tension, and inertia-dominated regimes.

Characteristic		Dominating forces		
		Viscosity	Surface tension	Inertia
Indicator	Trajectory	rectilinear	helical-to-zigzag	zigzag
	$v_t - D_e$ trend	increasing	decreasing	increasing
	$E - D_e$ trend	decreasing	constant	constant
Effect on v_t	Effect of μ_0	significant	less significant	insignificant
	Effect of p and λ	insignificant	insignificant	significant for non-Newtonian systems
	Effect of E	more significant for less viscous systems	significant	significant for non-Newtonian systems

CRediT authorship contribution statement

Hauna Fathmadinda Hosen: Writing – review & editing, Writing – original draft, Visualization, Validation, Software, Methodology, Investigation, Formal analysis, Data curation, Conceptualization. **Armin Shahmardi:** Writing – review & editing, Writing – original draft, Visualization, Software, Methodology, Investigation, Data curation, Conceptualization. **Luca Brandt:** Writing – review & editing, Supervision, Resources, Conceptualization. **Jannike Solsvik:** Writing – review & editing, Supervision, Resources, Project administration, Funding acquisition, Conceptualization.

Declaration of competing interest

The authors declare that they have no known competing financial interests or personal relationships that could have appeared to influence the work reported in this paper.

Data availability

Data will be made available on request.

Acknowledgments

The work was supported by the Research Council of Norway under SFI Industrial Biotechnology Research Center (Grant no. 978662112). Computational time was provided by the Norwegian Research Infrastructure Services (NRIS, Pr. NN9561K).

Appendix A. Model fitting for Newtonian cases

This appendix presents the comparison between different semi-empirical models (Fan and Tsuchiya, 1990; Maneri and Vassallo, 2000; Baz-Rodríguez et al., 2012; Tomiyama et al., 2002) fitted to different

Table A.1
Fluid properties and fitted model parameters for this work and comparable systems in the existing literature.

System	Reference	ρ(kg/m^3)	μ(Pa s)	σ(mN/m)	Mo	Fan			Baz		Maneri	
						c	K_{b0}	n	K_b	n	K	n
Glycerol, $\mu \approx 0.10$ Pa s	Raymond and Rosant (2000)	1222.00	1.60E−01	63.00	2.10E−02	1.4	10.2	1.4	28.3	2.2	14.4	2.1
	Liu et al. (2016)	1220.30	1.15E−01	66.00	4.93E−03	1.4	14.2	1.4	46.2	2.5	21.6	2.2
	Ravisankar et al. (2022)	1222.60	1.10E−01	71.89	3.16E−03	1.4	11.9	1.7	31.6	2.7	18.0	2.7
	Current work, glycerol 86%	1223.27	1.10E−01	60.01	4.08E−03	1.4	14.7	1.8	41.0	3.5	21.1	3.2
Glycerol, $\mu \approx 0.07$ Pa s	Maxworthy et al. (1996)	1208.50	6.01E−02	65.50	3.76E−04	1.4	9.4	1.8	25.8	3.1	18.2	3.1
	Raymond and Rosant (2000)	1205.00	7.50E−02	64.00	9.81E−04	1.4	9.5	1.5	21.9	1.9	16.2	2.1
	Liu et al. (2016)	1206.50	6.30E−02	67.00	4.25E−04	1.4	14.7	1.3	44.8	1.9	26.7	1.9
	Current work, glycerol 82%	1213.00	6.80E−02	59.88	5.74E−04	1.4	17.3	2.0	49.0	3.9	27.6	3.3
Glycerol, $\mu \approx 0.01$ Pa s	Bryn (1949)	1143.00	9.15E−03	69.90	1.76E−07	1.4	0.3	11.4	531.0	0.5	111.3	0.4
	Maxworthy et al. (1996)	1153.80	9.45E−03	67.82	2.17E−07	1.4	2.3	13.2	37.0	3.2	41.2	4.1
	Raymond and Rosant (2000)	1150.00	1.30E−02	64.00	9.27E−07	1.4	18.2	3.8	47.1	5.6	44.0	7.3
	Aoyama et al. (2016)	1155.00	9.80E−03	67.00	2.60E−07	1.4	12.0	2.3	31.0	2.7	36.0	3.5
	Current work, glycerol 60%	1153.71	1.10E−02	56.06	3.98E−07	1.4	25.0	1.7	70.0	2.0	70.0	2.9
Water	Uppermost data	998.00	1.00E−03	72.80	2.54E−11	1.2	14.7	4.8	36.0	4.8	110.0	22.0
	Lowermost data	998.00	1.00E−03	72.80	2.54E−11	1.2	14.7	0.6	36.0	0.5	110.0	0.6
	Current work,$_{\text{statistically treated}}$	998.00	1.00E−03	72.80	2.54E−11	0.85	14.7	3.75	12.0	0.75	42.0	6.66

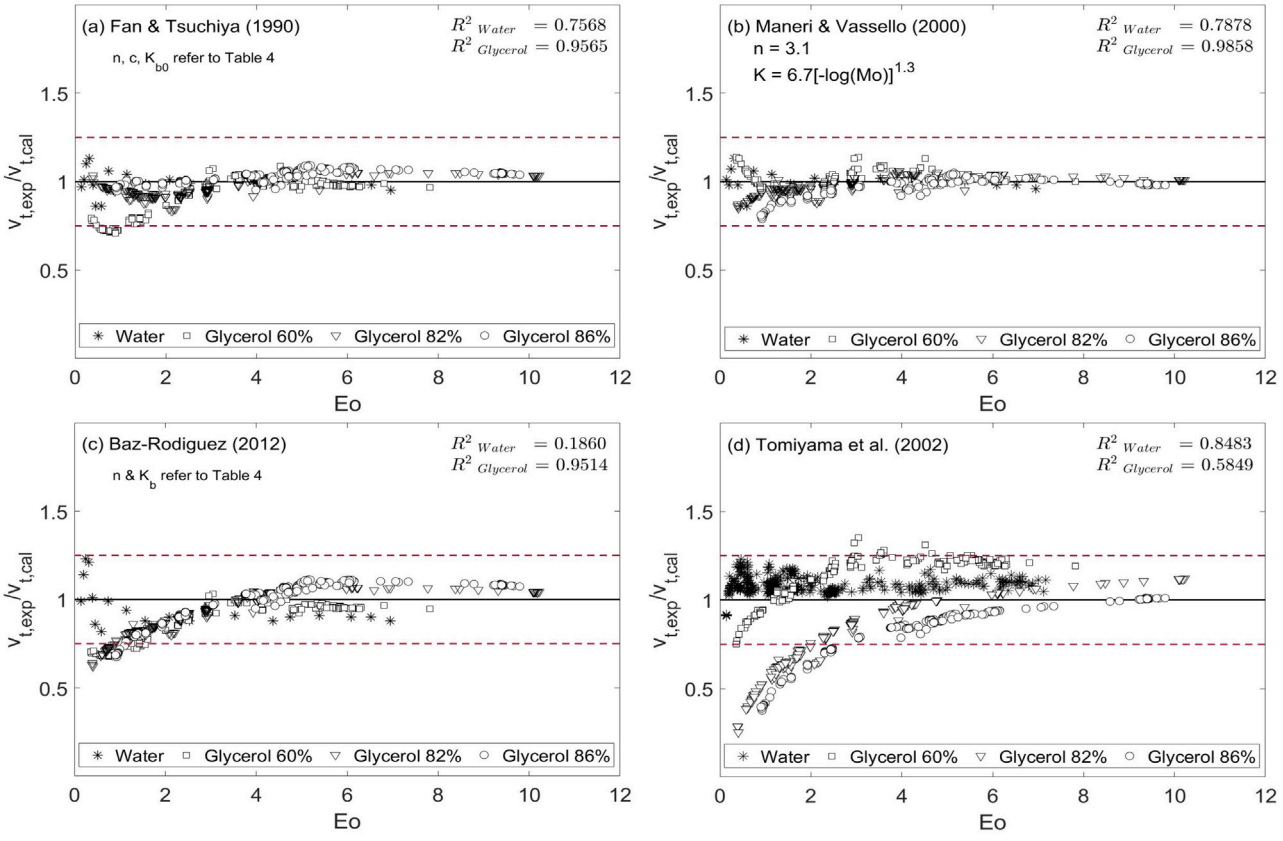

Fig. A.1. The ratio of experimental to calculated velocities as a function of Eötvös number for different Newtonian systems. The red dashed-lines represent ± 25% of the true value. (a) and (c) are the fitted models where the parameter values for each case are summarized in Table A.1. (b) is the adjusted model with $n = 3.1$ and $K = 6.7(-\log(Mo))^{1.3}$ as the fitted parameter values. (d) is the original expression suggested by Tomiyama et al. (2002). R^2 is the coefficient of determination which represents the goodness of fit.

experimental data (Raymond and Rosant, 2000; Liu et al., 2016; Ravisankar et al., 2022; Maxworthy et al., 1996; Bryn, 1949; Aoyama et al., 2016). The model parameters and the corresponding fluid properties are listed in Table A.1. The uppermost and lowermost data are obtained by extracting the highest and lowest terminal velocities in Fig. 9. According to Fig. A.1, the Maneri and Vassallo (2000)'s model fits the experimental data with the highest accuracy.

Appendix B. Model fitting for shear-thinning fluids assuming $\dot{\gamma} = v/D_e$

This appendix considers $\dot{\gamma} = v/D_e$ in the estimation of the apparent viscosity for shear-thinning cases. The estimated viscosity is used to evaluate different expressions for the terminal velocity suggested

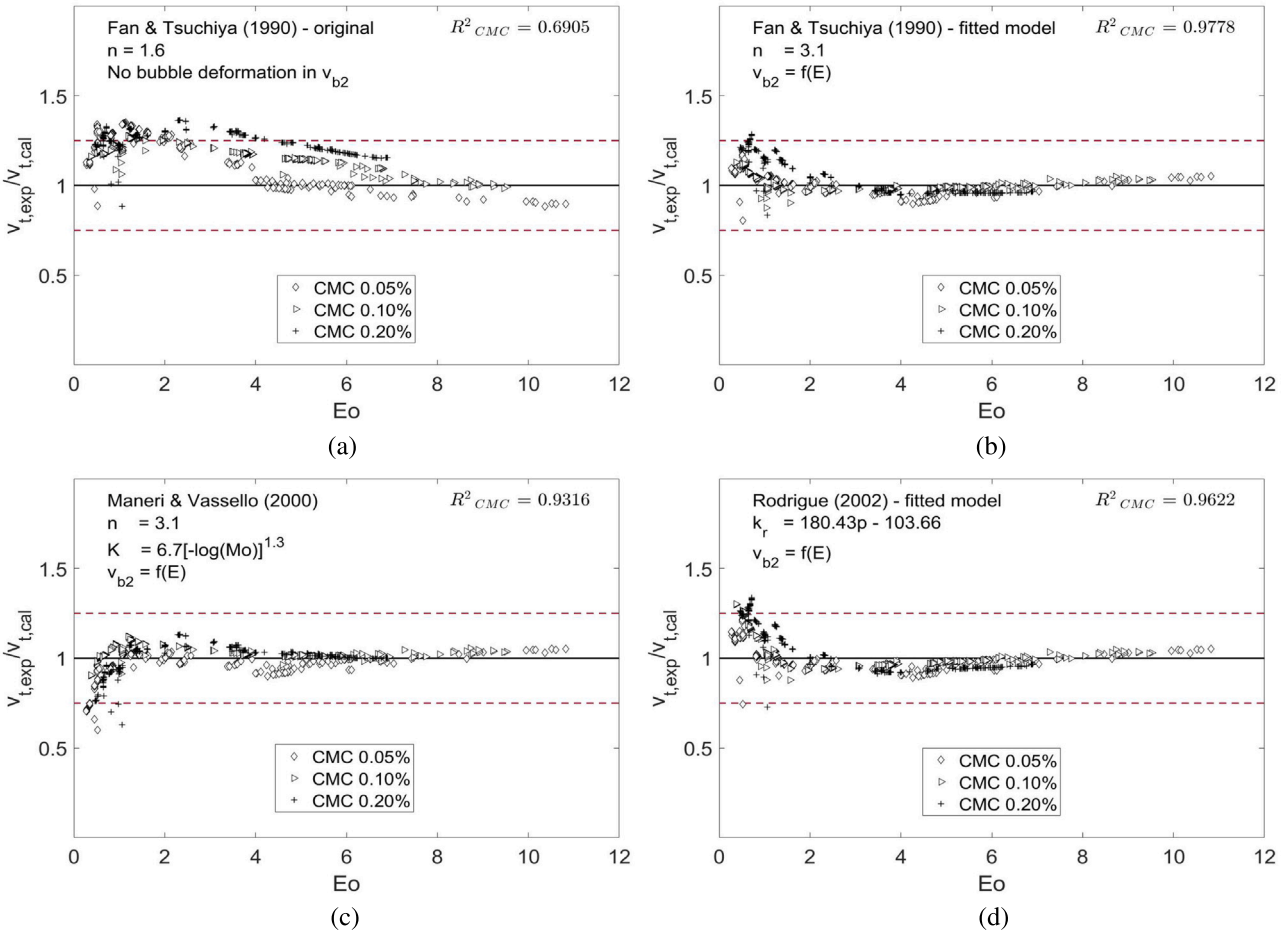

Fig. B.1. The ratio of experimental to calculated velocities as a function of Eötvös number for different CMC solutions. The red dashed-lines represent ± 25% of the true value.

Table B.1
Fitted expression of Maneri and Vassallo (2000).

Maneri and Vassallo (2000)	Modified Term
$v_t = \left[\frac{1}{v_{b1}{}^n} + \frac{1}{v_{b2}{}^n}\right]^{-1/n}$	–
$v_{b1} = \frac{\rho_l g D_e^2}{K_b \mu_l}$	–
$v_{b2} = \sqrt{\frac{2c\sigma}{\rho_l D_e} + \frac{gD_e}{2}}$	$v_{b2} = \sqrt{\frac{2c\sigma}{\rho_l D_e} E^p + \frac{gD_e}{2}\frac{E^{f(p)}}{1-E^2}}$ $f(p) = 8234.3\, p^{23.8}$
$K_b = K\left(1.0 - e^{-5.31\times10^{10} Mo}\right)\left(\frac{D_e}{D_o}\right)^a$	–
$D_o = 2.0\left[\frac{\sigma}{\Delta\rho g}\right]^{1/2}$	–
$a = 0.425$	–
$K = 148$ or 60	$K = 6.7\left[-\log(Mo)\right]^{1.3}$
$c = 1.0$ or 1.4	–
$n = 8.0$	$n = 3.1$

by Fan and Tsuchiya (1990), Maneri and Vassallo (2000), and Rodrigue (2002), as presented in Table 1. The ratio of the experimental to the computed velocities is plotted against the Eötvös number in Fig. B.1. The highest coefficient of determination, $R^2 = 0.9778$, is obtained with Fan and Tsuchiya (1990)'s expression after including the bubble deformation in their second term, i.e., $v_{b2} = f(E)$. However, R^2 for this case is still slightly lower than the Maneri and Vassallo (2000)'s expression presented in Fig. 16, with $R^2 = 0.9883$, where the viscosity is estimated by the empirical expression in Eq. (9).

The expression by Maneri and Vassallo (2000) is modified with the inclusion of the Morton number. For non-Newtonian fluids, the bubble aspect ratio and the power-law index are taken into account, as expressed in Table B.1.

Appendix C. Rheology parameters for comparable experimental results

The rheology parameters for non-Newtonian fluids that correspond to Fig. 13 are listed in Table C.1.

Table C.1
Rheology parameters corresponding to experimental results in Fig. 13.

Reference	Fluid	p	λ(s)	μ_0(Pa s)	Remarks
Current work	CMC 0.05 wt% in water	0.7142	0.12	0.022	
$\mu = \mu_0\left[1 + (\lambda\dot{\gamma})^2\right]^{\frac{p-1}{2}}$	CMC 0.10 wt% in water	0.7057	0.11	0.030	
	CMC 0.20 wt% in water	0.6845	0.24	0.090	
Amirnia et al. (2013)	CMC 0.40 wt% in water	0.71	0.029	0.056	$m = 1.5$
$\mu = \mu_0\left[1 + (\lambda\dot{\gamma})^m\right]^{\frac{p-1}{m}}$	XG 0.11 wt% in water	0.39	4.1	0.42	$m = 1.0$
	XG 0.13 wt% in water	0.396	4.3	0.46	$m = 1.2$
	XG 0.15 wt% in water	0.346	5.8	0.94	$m = 1.0$
Xu et al. (2019)	XG 0.10 wt% in water	0.47	15.12	0.36	$\mu_\infty = 0.001$
$\frac{\mu-\mu_\infty}{\mu_0-\mu_\infty} = \left[1 + (\lambda\dot{\gamma})^2\right]^{\frac{p-1}{2}}$					

Appendix D. Simulations vs experiments for different cases

This appendix presents the details of the comparison between the simulations and the experiments. The comparison with the semi-empirical models and the literature data is also included for some cases. Fig. D.1 presents the data for small bubbles. The subscripts sim, exp, lit, and mod respectively refer to the results obtained from the simulation, experiment, literature, and model. The symbols $\Delta v_{t,exp}$, $\Delta v_{t,lit}$, and $\Delta v_{t,mod}$ describe the deviation in terminal velocity obtained

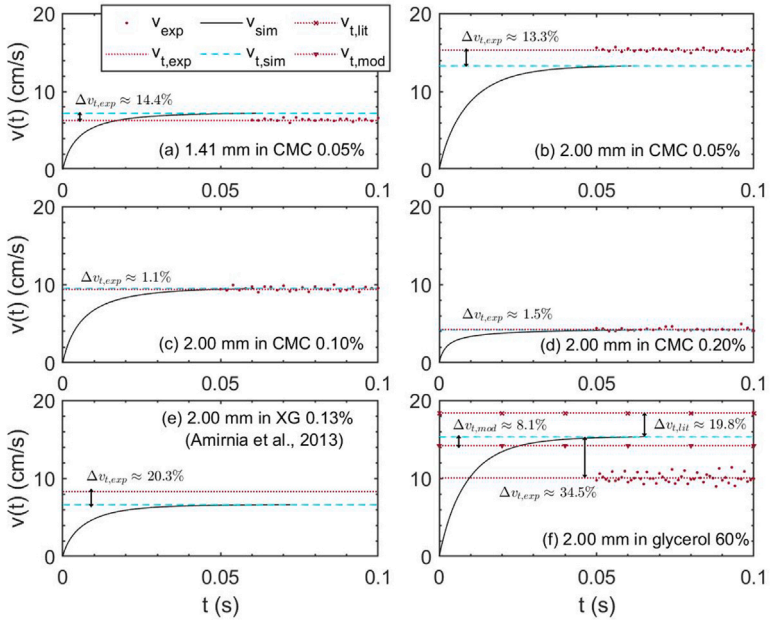

Fig. D.1. Vertical velocity obtained for (a) D_e = 1.41 mm and (b)–(f) D_e = 2 mm in various solutions according to Table 4. Solid line: simulation, dashed-line: terminal velocity estimated from simulation, dots: experiment, dotted-line: terminal velocity estimated from experiment, ×: terminal velocity estimated by Aoyama et al. (2016), ▽: terminal velocity estimated by Fan and Tsuchiya (1990)'s model.

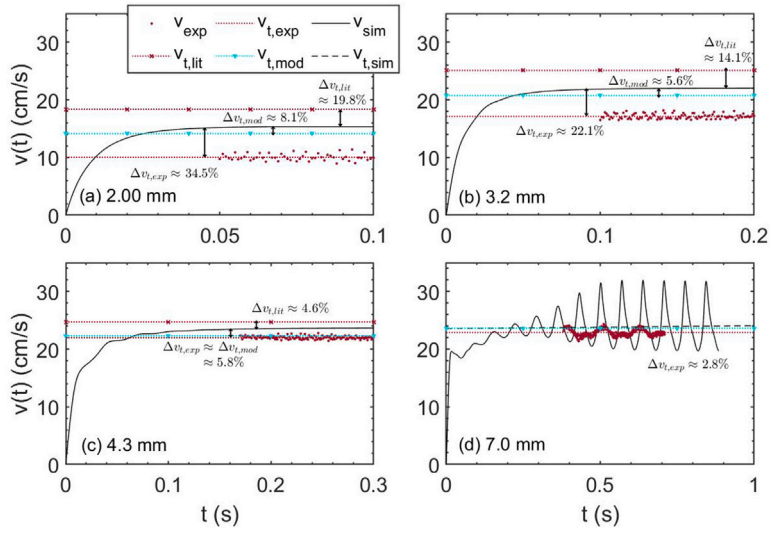

Fig. D.2. Vertical velocity obtained for (a) D_e = 2.0 mm, (b) D_e = 3.2 mm, (c) D_e = 4.3 mm, and (d) D_e = 7.0 mm in Glycerol 60%. Solid line: simulation, dashed-line: terminal velocity estimated from simulation, dots: experiment, dotted-line: terminal velocity estimated from experiment, ×: terminal velocity estimated by Aoyama et al. (2016) for (a)–(b) and Raymond and Rosant (2000) for (c), ▽: terminal velocity estimated by Fan and Tsuchiya (1990)'s model.

from the experiment, the literature, and the model compared to the simulation results.

The large deviation in Fig. D.1 (f) is similarly observed for the literature data of Aoyama et al. (2016). These differences decrease when the bubbles are larger, as observed in Fig. D.2.

Figs. D.3–D.4 present the comparison of v_t, D_e and E for large bubbles. In both figures, the simulation for cases (a), (b) and (f) tends to oscillate at the terminal state, i.e., after $t \approx 0.4$ s. These oscillations seem to exhibit the same physical behavior obtained in the experimental results, especially when the liquid medium is less viscous. Fig. D.3 shows that the v_t values are fairly comparable for all cases where the highest deviation values, Δv_t = 14.7% and Δv_t = 17.7%, are obtained for the lowest CMC concentration. The deviation of D_e for all cases in Fig. D.4 lies between 9% – 13% which looks reasonable, considering that the experimental images were obtained at different angles that may affect the projected area of the bubble and eventually the averaged D_e. This effect, however, seems to influence the deviation in E more significantly with a difference in the range of 2.5% – 38.1%. Notice that, due to unavailable data in Amirnia et al. (2013), the aspect ratio E in Fig. D.4 (e) is taken as the same E for CMC 0.10% in the current work, Fig. D.4 (c), considering that both cases have the same terminal velocity within $D_e \approx 1.5 - 7.0$ mm. The visual comparison of the bubble shape is presented in Figs. 18–19.

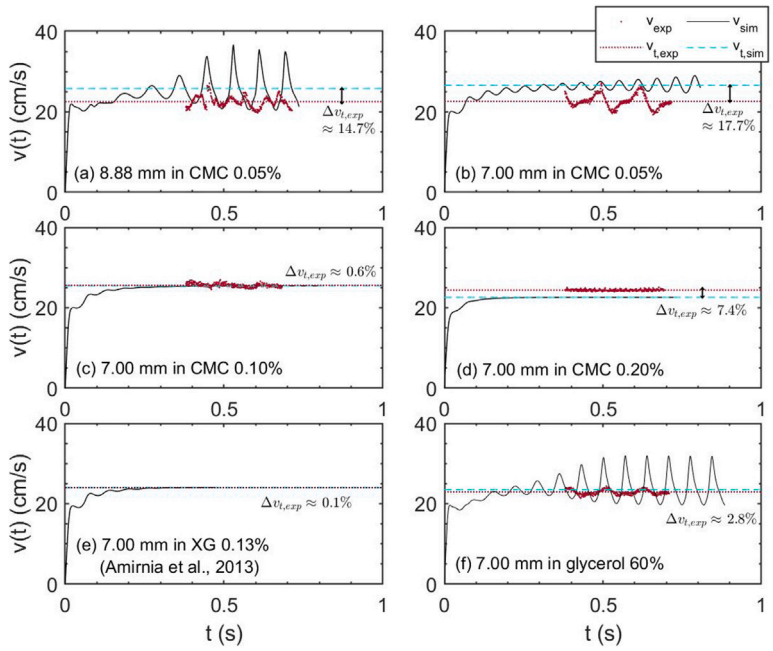

Fig. D.3. Vertical velocity obtained for (a) $D_e = 8.88$ mm and (b)–(f) $D_e = 7$ mm in various solutions according to Table 4. Solid line: simulation, dashed-line: terminal velocity estimated from simulation, dots: experiment, dotted-line: terminal velocity estimated from experiment.

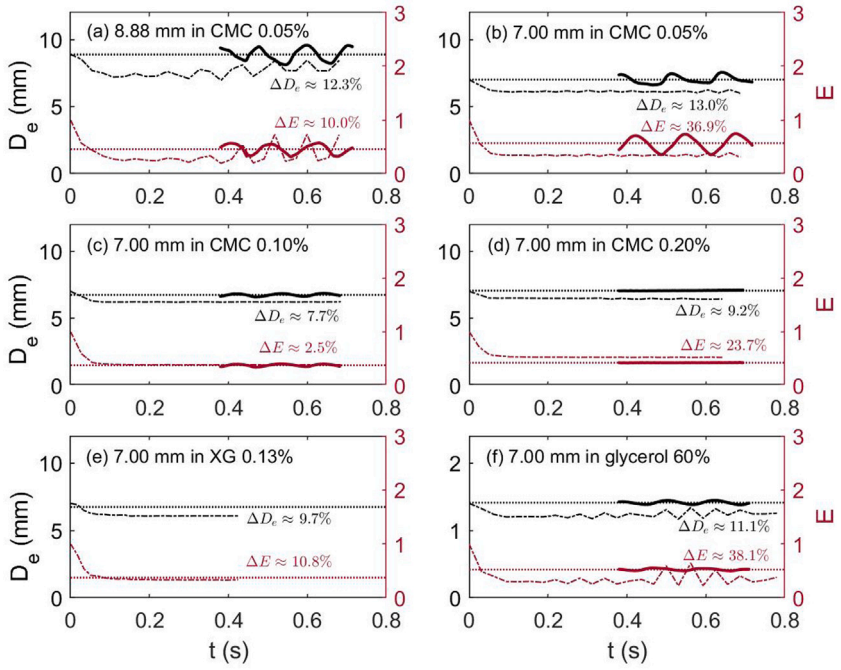

Fig. D.4. Time evolution of D_e and E for (a) $D_e = 8.88$ mm and (b) – (f) $D_e = 7$ mm in various solutions according to Table 4. Dotted-dashed line: simulation, solid line: experiment, dotted-line: averaged experimental value.

References

Amirnia, S., de Bruyn, J.R., Bergougnou, M.A., Margaritis, A., 2013. Continuous rise velocity of air bubbles in non-Newtonian biopolymer solutions. Chem. Eng. Sci. 94, 60–68.

Aoyama, S., Hayashi, K., Hosokawa, S., Tomiyama, A., 2016. Shapes of ellipsoidal bubbles in infinite stagnant liquids. Int. J. Multiph. Flow 79, 23–30.

Barba, F.C., Rodríguez-Jasso, R.M., Sukumaran, R.K., Ruiz, H.A., et al., 2022. High-solids loading processing for an integrated lignocellulosic biorefinery: Effects of transport phenomena and rheology–A review. Bioresour. Technol. 127044.

Barnes, H.A., Hutton, J.F., Walters, K., 1989. An Introduction to Rheology. Vol. 3, Elsevier.

Battistella, A., van Schijndel, S., Baltussen, M., Roghair, I., van Sint Annaland, M., 2020. On the terminal velocity of single bubbles rising in non-Newtonian power-law liquids. J. Non-Newton. Fluid Mech. 278, 104249.

Baz-Rodríguez, S., Aguilar-Corona, A., Soria, A., 2012. Rising velocity for single bubbles in pure liquids. Revista Mexicana De Ingeniería Química 11 (2), 269–278.

Bazesefidpar, K., Brandt, L., Tammisola, O., 2022. Numerical simulation of the coalescence-induced polymeric droplet jumping on superhydrophobic surfaces. J. Non-Newton. Fluid Mech. 307, 104872.

Brackbill, J.U., Kothe, D.B., Zemach, C., 1992. A continuum method for modeling surface tension. J. Comput. Phys. 100 (2), 335–354.
Bryn, T., 1949. Speed of Rise of Air Bubbles in Liquids. Report No. 132, David Taylor Model, Basin.
Celata, G.P., D'Annibale, F., Di Marco, P., Memoli, G., Tomiyama, A., 2007. Measurements of rising velocity of a small bubble in a stagnant fluid in one-and two-component systems. Exp. Therm Fluid Sci. 31 (6), 609–623.
Chehata, D., 2004. Estudio De La Discontinuidad En La Velocidad De Ascenso De Una Burbuja En Un Liquido No-Newtoniano (MSc Thesis). Univ.Nac.Auton.Mex.
Chhabra, R.P., 2007. Bubbles, Drops, and Particles in Non-Newtonian Fluids. Taylor & Francis.
Cifani, P., 2019. Analysis of a constant-coefficient pressure equation method for fast computations of two-phase flows at high density ratios. J. Comput. Phys. 398, 108904.
Clift, R., 1978. Bubbles, Drops and Particles. Academic Press.
Clift, R., Gauvin, W., 1971. Motion of entrained particles in gas streams. Can. J. Chem. Eng. 49 (4), 439–448.
Crialesi-Esposito, M., Scapin, N., Demou, A.D., Rosti, M.E., Costa, P., Spiga, F., Brandt, L., 2023. FluTAS: A GPU-accelerated finite difference code for multiphase flows. Comput. Phys. Comm. 284, 108602.
Darmana, D., Deen, N., Kuipers, J., Harteveld, W., Mudde, R., 2009. Numerical study of homogeneous bubbly flow: influence of the inlet conditions to the hydrodynamic behavior. Int. J. Multiph. Flow 35 (12), 1077–1099.
De Vries, A., Biesheuvel, A., Van Wijngaarden, L., 2002. Notes on the path and wake of a gas bubble rising in pure water. Int. J. Multiph. Flow 28 (11), 1823–1835.
Dewsbury, K., Karamanev, D., Margaritis, A., 1999. Hydrodynamic characteristics of free rise of light solid particles and gas bubbles in non-Newtonian liquids. Chem. Eng. Sci. 54 (21), 4825–4830.
Dodd, M.S., Ferrante, A., 2014. A fast pressure-correction method for incompressible two-fluid flows. J. Comput. Phys. 273, 416–434.
Doran, P.M., 2013. Bioprocess Engineering Principles. Elsevier.
Fan, L.-S., Tsuchiya, K., 1990. Bubble Wake Dynamics in Liquids and Liquid-Solid Suspensions. Butterworth-Heinemann.
Haberman, W.L., Morton, R., 1953. An Experimental Investigation of the Drag and Shape of Air Bubbles Rising in Various Liquids. Technical report, David Taylor Model, Basin, Washington, DC.
Hassan, N., Khan, M.M.K., Rasul, M., et al., 2008. A study of bubble trajectory and drag coefficient in water and non-Newtonian fluids. WSEAS Trans. Fluid Mech. 3 (261), e270.
Ishii, M., Chawla, T., 1979. Local Drag Laws in Dispersed Two-Phase Flow. Technical report, Argonne National Lab., IL (USA).
Islam, M.T., Ganesan, P.B., Cheng, J., Uddin, M.S., 2020. Single bubble rising behaviors in Newtonian and non-Newtonian fluids with validation of empirical correlations: A computational fluid dynamics study. Eng. Rep. 2 (1), e12100.
Jain, S.S., 2022. Accurate conservative phase-field method for simulation of two-phase flows. J. Comput. Phys. 469, 111529.
Kure, I.K., Jakobsen, H.A., La Forgia, N., Solsvik, J., 2021. Experimental investigation of single bubbles rising in stagnant liquid: Statistical analysis and image processing. Phys. Fluids 33 (10), 103611.
Levich, V.G., 1962. Physicochemical Hydrodynamics. Prentice-Hall Inc.
Li, S., Fan, J., Li, R., Wang, L., Luan, J., 2018. Effect of surfactants on hydrodynamics characteristics of bubble in shear thinning fluids at low Reynolds number. J. Cent. South Univ. 25 (4), 805–811.
Li, S., Ji, J., Liu, Z., 2022. The shape and drag coefficient for a single bubble rising in stagnant shear-thinning viscoelastic liquids. Exp. Therm Fluid Sci. 133, 110597.
Li, S., Ma, Y., Jiang, S., Fu, T., Zhu, C., Li, H.Z., 2012. The drag coefficient and the shape for a single bubble rising in non-Newtonian fluids. J. Fluids Eng. 134 (8).
Liu, L., Yan, H., Zhao, G., 2015. Experimental studies on the shape and motion of air bubbles in viscous liquids. Exp. Therm Fluid Sci. 62, 109–121.
Liu, L., Yan, H., Zhao, G., Zhuang, J., 2016. Experimental studies on the terminal velocity of air bubbles in water and glycerol aqueous solution. Exp. Therm Fluid Sci. 78, 254–265.
Lunde, K., Perkins, R.J., 1998. Shape oscillations of rising bubbles. In: Fascination of Fluid Dynamics. Vol. 45, Springer, pp. 387–408.
Mahmoudi, S., Hashemi Shahraki, B., Aghajani, M., 2019. Experimental and theoretical investigation of CO_2 and air bubble rising velocity through kerosene and distilled water in bubble column. J. Dispers. Sci. Technol. 40 (1), 33–42.
Mahmoudi, S., Hemmatian, F., Dahkaee, K.P., Hlawitschka, M.W., Kantzas, A., 2022. Detailed study of single bubble behavior and drag correlations in Newtonian and non-Newtonian liquids for the design of bubble columns. Chem. Eng. Res. Des. 179, 119–129.
Maneri, C.C., Vassallo, P.F., 2000. Dynamics of bubbles rising in finite and infinite media. In: Fluids Engineering Division Summer Meeting. Vol. 36967, pp. 1811–1828.
Mastropietro, D.J., Nimroozi, R., Omidian, H., 2013. Rheology in pharmaceutical formulations-a perspective. J. Dev. Drugs 2 (2), 1–6.
Maxworthy, T., Gnann, C., Kürten, M., Durst, F., 1996. Experiments on the rise of air bubbles in clean viscous liquids. J. Fluid Mech. 321, 421–441.
Mendelson, H.D., 1967. The prediction of bubble terminal velocities from wave theory. AIChE J. 13 (2), 250–253.
Oshaghi, M.R., Shahsavari, M., Afshin, H., Firoozabadi, B., 2019. Experimental investigation of the bubble motion and its ascension in a quiescent viscous liquid. Exp. Therm Fluid Sci. 103, 274–285.
Pang, M., Lu, M., 2018. Numerical study on dynamics of single bubble rising in shear-thinning power-law fluid in different gravity environment. Vacuum 153, 101–111.
R. P. Chhabra, J.F.R., 2008. Non-Newtonian Flow and Applied Rheology. Elsevier.
Ravisankar, M., Correa, A.G., Su, Y., Zenit, R., 2022. Hydrodynamic interaction of a bubble pair in viscoelastic shear-thinning fluids. J. Non-Newton. Fluid Mech. 309, 104912.
Raymond, F., Rosant, J.-M., 2000. A numerical and experimental study of the terminal velocity and shape of bubbles in viscous liquids. Chem. Eng. Sci. 55 (5), 943–955.
Rodrigue, D., 2001. Generalized correlation for bubble motion. AIChE J. 47 (1), 39–44.
Rodrigue, D., 2002. A simple correlation for gas bubbles rising in power-law fluids. Can. J. Chem. Eng. 80 (2), 289–292.
Rodrigue, D., De Kee, D., Fong, C.C.M., 1999. The slow motion of a single gas bubble in a non-Newtonian fluid containing surfactants. J. Non-Newton. Fluid Mech. 86 (1–2), 211–227.
Rutz, D., Janssen, R., 2007. Biofuel technology handbook. WIP Renew. Energies 95.
Rybczynski, W., 1911. Uber die fortschreitende Bewegung einer flussigen Kugel in einem zahen Medium. Bull. Acad. Sci. Cracovie A 1, 40–46.
Scapin, N., Shahmardi, A., Chan, W., Jain, S., Mirjalili, S., Pelanti, M., Brandt, L., 2022. A mass-conserving pressure-based method for two-phase flows with phase change. In: Center for Turbulence Research Proceedings of the Summer Program 2022.
Soto, E., 2008. Flow of Single Air Bubbles in Complex Fluids (Ph.D. thesis). Univ.Nac.Auton.Mex.
Stokes, G.G., et al., 1851. On the Effect of the Internal Friction of Fluids on the Motion of Pendulums. Pitt Press, Cambridge.
Tagawa, Y., Takagi, S., Matsumoto, Y., 2014. Surfactant effect on path instability of a rising bubble. J. Fluid Mech. 738, 124–142.
Tomiyama, A., Celata, G., Hosokawa, S., Yoshida, S., 2002. Terminal velocity of single bubbles in surface tension force dominant regime. Int. J. Multiph. Flow 28 (9), 1497–1519.
Wenyuan, F., Youguang, M., Shaokun, J., Ke, Y., Huaizhi, L., 2010. An experimental investigation for bubble rising in non-Newtonian fluids and empirical correlation of drag coefficient. J. Fluids Eng. 132 (2).
Wu, M., Gharib, M., 2002. Experimental studies on the shape and path of small air bubbles rising in clean water. Phys. Fluids 14 (7), L49–L52.
Xu, F., Midoux, N., Li, H.-Z., Hébrard, G., Dietrich, N., 2019. Characterization of bubble shapes in non-Newtonian fluids by parametric equations. Chem. Eng. Technol. 42 (11), 2321–2330.
Zenit, R., Feng, J., 2018. Hydrodynamic interactions among bubbles, drops, and particles in non-Newtonian liquids. Annu. Rev. Fluid Mech. 50, 505–534.
Zenit, R., Magnaudet, J., 2009. Measurements of the streamwise vorticity in the wake of an oscillating bubble. Int. J. Multiph. Flow 35 (2), 195–203.
Zhang, A., Su, D., Li, C., Zhang, Y., Jiang, B., Pan, F., 2022. Investigation of bubble dynamics in a micro-channel with obstacles using a conservative phase-field lattice Boltzmann method. Phys. Fluids 34 (4), 043312.
Zhang, L., Yang, C., Mao, Z.-S., 2008a. An empirical correlation of drag coefficient for a single bubble rising in non-Newtonian liquids. Ind. Eng. Chem. Res. 47 (23), 9767–9772.
Zhang, L., Yang, C., Mao, Z.-S., 2008b. Unsteady motion of a single bubble in highly viscous liquid and empirical correlation of drag coefficient. Chem. Eng. Sci. 63 (8), 2099–2106.
Zhang, L., Yang, C., Mao, Z.-S., 2010. Numerical simulation of a bubble rising in shear-thinning fluids. J. Non-Newton. Fluid Mech. 165 (11–12), 555–567.